Initiation and development of a mesoscale convective system in the Ebro River Valley and related heavy precipitation over northeastern Spain during HyMeX IOP 15a

Keun-Ok Lee, Cyrille Flamant, Véronique Ducrocq, Fanny Duffourg, Nadia Fourrié, Julien Delanoë, Joan Bech

Initiation and development of a mesoscale convective system in the Ebro River Valley and related heavy precipitation over north-eastern Spain during HyMeX IOP 15a

K.-O, Lee[1†], C. Flamant[1], V. Ducrocq[2], F. Duffourg[2], N. Fourrié[2], J. Delanoë[1], J. Bech[3]

[1]LATMOS/IPSL, UPMC Université. Paris 06, Sorbonne Universités, UVSQ, CNRS, Paris, France

[2]CNRM, UMR 3589, Météo-France and CNRS, Toulouse, France

[3]Department of Astronomy and Meteorology, University of Barcelona, Barcelona, Spain

ABSTRACT

During Intensive Observation Period 15a (20 October 2012) of the first Special Observation Period of the Hydrological cycle in the Mediterranean Experiment, north-eastern Spain experienced heavy precipitation (130 mm in 24 h) associated with a retrograde regeneration mesoscale convective system (MCS) developing in the exit region of the Ebro River Valley (ERV). The life cycle of the MCS that brought intense hourly rainfall (34 mm) from the foothill of Iberian Plateau to the central Pyrenees, as well as the detailed structure of moist marine flow upstream, were analysed using a combination of ground-based, airborne and space-borne observations as well as model analyses. Over the Balearic Sea, the south-westerlies along the north-eastern flank of a surface low converged with south-easterlies from north Africa, creating a near surface moisture tongue in the region of the Balearic Islands, and a southeast-northwest oriented convergence line within a cloud cluster advecting from northern Africa. Airborne lidar measurements, acquired upstream of the ERV, evidenced water vapour mixing ratios in excess of 15 g kg^{-1} in the marine atmospheric boundary layer. In the mid-level (700 hPa), the presence of an elevated moisture plume from tropical Africa contributed for about one third to the large moisture content present over the western Mediterranean Sea. In this moist environment, the MCS was initiated over the orography of the north-eastern tip of the Iberian plateau, due to the combined influence of the approaching convergence line ahead of the surface low and the convergence resulting from weak north-

[†]*Corresponding author*: LATMOS/IPSL, 4 Place Jussieu, 75252 Paris, France E-mail: keun-ok.lee@latmos.ipsl.fr

westerlies channeled in the ERV and the easterlies impinging on the coastal range. After the initiation phase, the MCS further developed over the foothill of Iberian Plateau and moved into the ERV and along the southern flank of the Pyrenees, thanks to the penetration of the warm and moist maritime south-easterly flow through the narrow gap between the north-eastern part of the Iberian Plateau and the Catalan coastal range.

Running head*: Initiation and development of a MCS over the Ebro River Valley*

Keywords*: Balearic Sea, Iberian Plateau, moisture tongue, orographic forcing, flow convergence, synoptic forcing*

1. Introduction

The Western Mediterranean coastal regions are frequently affected by heavy precipitation that produces flash floods and landslides (e.g. Ricard *et al.* 2012; Llasat *et al.* 2013). The mountainous terrain around the Western Mediterranean Sea (e.g. the Pyrenees, Massif Central, Alps, Apennines, and Atlas), but also the numerous islands (Balearic Islands, Corsica, Sardinia and Sicily), favour convective initiation and heavy precipitation events (HPEs) due to orographic forcing. The lifting of the conditionally unstable low-level marine flow impinging upon the foothills bordering the western Mediterranean Sea is a well-known mechanism for convection triggering (Rotunno and Houze, 2007; Nuissier *et al*. 2008; Ricard *et al*. 2012; Trapero *et al*. 2013a, 2013b).

In particular, the north-eastern coastal region of the Iberian Peninsula experiences frequent torrential rains (defined when at least 2 % of the stations register more than 50 mm of precipitation in 24 h, e.g. Romero *et al*. 1999) able to produce flash floods in the area as illustrated by the fact that 100 mm h^{-1} rainfall rates have a 1 year return period for Barcelona city, according to a climatological analysis carried out with a 5 min accumulated precipitation dataset covering 60 years (Lorente and Redaño, 1990). According to Romero *et al.* (1999), there are 3 main low-level flow regimes which lead to precipitation enhancement over eastern Spain, in connection with orography: F1) a westerly-to-southerly flow from the Atlantic over the whole Iberian Peninsula ahead/west of an approaching upper-level trough favouring rainfalls in north-eastern Spain; F2) a south-easterly flow from the east of a low over the south part of Spain leading to rainfall over the eastern flank of Spain; and F3) a northerly flow to the west of a low over the Gulf of Lion producing significant rainfall in the north-east of the Iberian Peninsula. However, the mesoscale processes by which convection is initiated and leads to HPEs for each of the 3 scenarios above can be quite diverse. In all cases, the transport of moist air masses towards the eastern Spanish mountains is a prerequisite for HPEs to occur in the Valencia or in the Barcelona area (Romero *et al*. 1999; Trapero *et al*. 2013a, 2013b). More generally, Duffourg and Ducrocq (2013) estimated that the evaporation from the Mediterranean accounts for about 40% of the water vapour feeding deep convection developing on the coastal mountains of southern France, downstream of the low-level marine flow (1−1.5 km deep). The Atlantic Ocean (Winschall *et al.* 2012) and tropical Africa (Turato *et al.* 2004; Chazette *et al.* 2016; Lee *et al*. 2016) have also been suggested as remote sources of moisture feeding for HPEs.

Previous studies have evidenced the synoptic ingredients for supplying moist air to deep convection (e.g. Romero *et al.* 1999; Nuissier *et al.* 2011; Ricard *et al.* 2012; Melani *et al.* 2013). They have stressed out the need for detailed information on the dynamics and moisture distribution associated with marine inflow upstream of deep convection, i.e. in areas where observations in the low-levels are scarce. Furthermore, convective initiation stemming from the marine flow interaction with the moderate to steep orography at the coast and further inland is very case-dependent because of the large variety of favourable dynamical and thermodynamical ingredients occurring in complex terrain. Hence, each case basically deserves to be analysed in its own right.

The first Special Observation Period (SOP1) of the Hydrological cycle in the Mediterranean Experiment (HyMeX, http://www.hymex.org/), which took place in Autumn 2012 aimed at improving knowledge on the origin and transport pattern of the moist air masses in pre-convective conditions and their link with HPEs (Ducrocq *et al.* 2014). During SOP1, dedicated ground-based, airborne and seaborne observation platforms were operated with the objective of documenting the interactions between HPEs forming in the coastal regions of Spain, France, and Italy, and the moist feeding flow over the Mediterranean where standard meteorological data are scarce.

In the present study, we focus on the HPE which occurred in north-eastern Spain during the Intense Observation Period (IOP) 15a on 20 October 2012 (Fig. 1a). During this IOP, a multi-cell V-shaped retrograde regeneration Mesoscale Convective System (MCS, hereafter named 'MCS B') formed in the exit region of the Ebro River Valley (ERV) (Fig. 2c). A multi-cell V-shaped retrograde regeneration MCS or back-building MCS is a MCS in which new development takes place on the upwind side. The new, more vigorous cells that form on the upwind side, replace older cells that continue to drift downwind. The topography surrounding the ERV consists of the Pyrenees (PY, in Fig. 1a) to the north, the Catalan coastal range (CA, in Fig. 1a) to the east and the Iberian Plateau (IB, in Fig. 1a) to the south. The Ebro River exits into the Balearic Sea, in the delta region, consisting of a narrow gap between the Catalan coastal range and the north-eastern part of the Iberian Plateau where terrain elevation can reach 1200 m above mean sea level -amsl. The typical altitude of the terrain surrounding the higher peaks in the north-eastern part of the Iberian Plateau (where MCS B was initiated) is between 500 and 1000 m amsl.

MCS B then propagated northward along the ERV with the synoptic southerly flow and impinged on the western and central Pyrenees leading to heavy precipitation (≥ 130 mm in 24 h) along the Valley and on the mountain range (Fig. 2d). Such V-shaped mesoscale convective systems are quite common in the Mediterranean region and have long been studied due to their capacity to produce heavy rain in a given location (McCann, 1983; Lee *et al.* 2016). The V-shape structure associated with these systems is generally observed in the satellite-derived brightness temperature fields. Following the description of McCann (1983), the lowest brightness temperature are observed at the apex of the V and a V-shaped region of slightly warmer brightness temperatures are seen to emanated from the apex following the wind direction at high levels.

During IOP 15a, a surface low moved north-eastward along the north-eastern coast of Spain, organizing a favourable flow regime for developing MCS with low-level south-easterly marine inflow and mid-level southerly flow over the exit region of the ERV. This flow regime was a mix of flow regimes F1 and F2 as defined by Romero *et al.* (1999). Previous studies have illustrated how the low-level south-easterly maritime inflow impinging over the Iberian Plateau is crucial for triggering MCS.

However due to the scarcity of humidity measurements over the sea, it is still unclear how the distribution of moisture in the south-easterly maritime flow is connected to MCSs development and life cycle in this coastal mountainous region. Here, this is investigated using the unprecedented wealth of data acquired during HyMeX SOP1, including measurements from two aircraft in addition to the standard observational networks and numerical weather prediction model analyses.

The observations and modelling tools used in this study are introduced in Section 2. The synoptic meteorological overview of IOP 15a is described in section 3, while the detailed analyses of the pre-convection environment, as well as the initiation phase and development phase of the MCS relevant to this study are provided in sections 4, 5 and 6, respectively. Finally the summary and conclusions of this study are given in Section 7.

2. Observational and modelling datasets

Unprecedented samplings of the dynamic and thermodynamic environments of HPEs in the western Mediterranean region were achieved during HyMeX SOP1 (Ducrocq *et al*. 2014). Details of the observational datasets used in this study and the AROME-WMED analysis data are provided in the following.

2.1. HyMeX SOP1 observational dataset

2.1.1. Surface networks

Hourly and 24-h accumulated rainfall data from the operational weather services over the HyMeX domain (western Mediterranean basin) were used, and the locations of the surface rain gauges (842 stations) over Spain and France are shown in Fig. 1. In addition, hourly surface automated weather station (AWS) data (260 stations) were employed to describe the near-surface (2 m above the surface) temperature field. Data from the operational radiosondes launched from Palma de Mallorca (Balearic Island, 2.7°E, 39.6°N) are also involved (see Fig. 1a for location). Hourly horizontal distribution of Total Integrated Water Vapour (TIWV) content was derived from a network of Global Positioning System (GPS) stations (Bock *et al.* 2016). Finally, total lightning (intra-cloud and cloud-to-ground) data, recorded by the total lightning location system composed by four LS-8000 Vaisala total lightning detectors operated by the meteorological service of Catalonia, was used (Pineda *et al*. 2011). In this study, we used data related to cloud-to-ground lightning to detect the most active convective cloud.

Near surface radar composite of reflectivity data (http://www.knmi.nl/opera) derived from French and Spanish operational radars with the temporal resolution of 15 min are also employed to track the location of heavy rainfall associated with a large number of and/or large size raindrops. In this study, reflectivity values in excess of 40 dBZ are used to identify the convective regions, while reflectivities over 35 dBZ are used to identify convective cells (e.g. Lee *et al*. 2012).

2.1.2. Dedicated HyMeX SOP 1 airborne observations

We used the water vapour lidar LEANDRE 2 embarked on-board the SAFIRE (Service des Avions Francais Instrumentés pour la Recherche en Environment) ATR42 aircraft to document the low-level moisture upstream of the MCS which formed near the Ebro River delta during the IOP 15a (ATR42 flight AS 52). The ATR42 flew from the French Mediterranean coast to the Balearic Islands from 0954 UTC to 1256 UTC on 20 October 2012 (black/blue solid line in Fig. 1a). LEANDRE 2 allowed measurements of the water vapour mixing ratio (WVMR) profiles with a precision ranging from less than 0.1 g kg^{-1} at 4.5 km above ground level to less than 0.4 g kg^{-1} near the surface (on average) for an along-beam resolution of 150 m (for the details, see Bruneau *et al*. 2001a, 2001b; Chazette *et al.* 2016; Di Girolamo *et al.* 2016; Duffourg *et al*. 2016; Flamant *et al*. 2015; Flaounas *et al.* 2016; Lee *et al.* 2016).

The SAFIRE Falcon 20 (F20) was also operated during IOP 15a. It embarked the RASTA Doppler cloud radar (Protat *et al*. 2004; Bousquet and Smull, 2006; Bouniol *et al.* 2008; Protat *et al.* 2009; Delanoë *et al.* 2013) and flew over the MCS B from 1320 UTC to 1630 UTC on 20 October 2012 (red solid line in Fig. 2d). The RASTA cloud radar (W-band, 95 GHz) has 6 beams (3 looking downward, 3 looking upward) measuring reflectivity and Doppler velocity along each radial, with a vertical coverage ranging from 0 to 15 km amsl. The reflectivity and Doppler velocity are measured with a vertical resolution of 60 m and a temporal resolution of 1.25 s. The minimal detectable cloud reflectivity is about

−35 dBZ, and the calibration accuracy is about 1−2 dB. The nadir reflectivity is calibrated using the ocean surface return technique (Li *et al.* 2005; Tanelli *et al*. 2008); Doppler velocity is corrected from folding and aircraft motion. The combination of at least 3 antennas (below or above the aircraft) allows us to retrieve the three components of the cloud wind field. Therefore cross-section of vertical velocity, cross track and along track winds are retrieved above and below the aircraft. The RASTA wind retrievals have been compared against ground based radar measurements in Bousquet *et al.* (2016). Note that the vertical velocity is the sum of the vertical air motion and the terminal fall velocity of the hydrometeors. Below the 0°C isotherm, precipitation mostly consists of rain and is not properly sampled by the cloud radar due to the attenuation by liquid precipitation at high frequencies (95 GHz) (Bousquet *et al.* 2016). Vertical air motion, in ice region (i.e. temperature < 0°C), is extracted from the vertical velocity using a variational approach which combines microphysical in-situ a priori information, radar Doppler velocity and reflectivity. This method has been developed for ice cloud only, as a result W is only retrieved for altitudes above the freezing level.

2.1.3. Space-borne observations

Calibrated thermal infrared Brightness Temperature (BT) data at 10.8 µm acquired every 5 min by the Spinning Enhanced Visible and Infrared Imager (SEVIRI) on-board the geostationary Meteosat Second Generation satellite (MSG) were used to investigate the evolution of deep convection. The spatial resolution of the MSG-SEVIRI data used is 0.05° in both latitude and longitude. The deep convective systems leading to heavy precipitation in the ERV domain were identified using SEVIRI BT at 10.8 µm together with lightning activity. Minima in BT are generally indicative of the cloud top overshoots associated with deep convection, and lower BT is seen in the region of taller convective cloud (e.g. Kato, 2006; Bedka, 2011). In this study, we identify deep convection using a criterion of BT of 210 K.

The moisture retrievals obtained from the Moderate Resolution Imaging Spectro-radiometer (MODIS) on-board the Aqua satellite were also employed (http://modis.gsfc.nasa.gov). The MODIS-derived TIWV contents and the Partial Integrated Water Vapour (PIWV) column between 700 hPa and 300 hPa levels were analysed in order to describe the distribution of moisture at the synoptic scale during the events.

The National Oceanic and Atmospheric Administration Oceansat-2 scatterometer (OSCAT, http://manati.star.nesdis.noaa.gov/products/OSCAT.php) ocean surface wind vector retrievals (level 2) at a spatial resolution of 12.5 km are employed to reveal the 10 m wind fields over the Balearic Sea on 20 October 2012. OSCAT crossed the Balearic Sea region once around 1300 UTC during the descending orbit.

2.2. Numerical model: AROME-WMED

To support the field campaign activities and to optimize flight planning during SOP1, a dedicated version of the operational convective-scale Application of Research to Operations at Mesoscale (AROME) was implemented (Fourrié *et al.* 2015). AROME is a regional non-hydrostatic and fully-compressible model. The HyMeX-dedicated configuration, AROME-WMED covers the Western Mediterranean basin with 2.5 km horizontal resolution and 60 vertical levels ranging from 10 m above ground to 1 hPa. A full description of AROME-WMED is provided by Fourrié *et al.* (2015).

A 3 h cycle data assimilation provides the initial atmospheric state of the AROME-WMED forecast. The lateral boundary conditions are updated hourly and provided by the French operational global model Action de Recherche Petite Echelle Grande Echelle (Courtier *et al.* 1991) forecasts. The AROME data assimilation system (Brousseau *et al.* 2008) based on a 3D variational algorithm applied, assimilates at 2.5 km horizontal resolution, data from radiosondes, aircraft, wind profilers, ships and buoys, surface stations (i.e. pressure, 2-m temperature and humidity, 10 m wind), GPS stations (i.e. zenithal total delays), radars over France (i.e. radar-derived winds and relative humidity derived from reflectivities), and SEVIRI (i.e. infrared radiances and satellite winds derived from atmospheric motion vectors) and from polar-orbiting satellites (infrared and micro-wave radiances, scatterometer wind surface) (Seity *et al*. 2011; Fourrié *et al.* 2015). Many important observing systems, such as AWSs, radar and SEVIRI data, are assimilated every 3 h. Moreover, observations from the HyMeX campaign (e.g. radiosondes, boundary layer pressurized balloons, ancillary surface data) were also assimilated in AROME-WMED.

Fourrié *et al*. (2015) showed that the overall performances of the AROME-WMED were good for the HyMeX SOP1 (mean 2-m temperature root mean square error (*RMSE*) of 1.7°C and mean 2-m relative humidity *RMSE* of 10%). Bock *et al*. (2016) highlighted a very good agreement for TIWV obtained with the AROME-WMED analyses and the GPS observations, with a small wet bias in the model (~0.3 kg m^{-2}) and a standard deviation of differences of ~1.6 kg m^{-2}.

In the present study, the AROME-WMED analysis data provided every 3 h are used together with observations to enhance our understanding of processes responsible for HPEs in the ERV.

3. IOP 15a overview

3.1. Synoptic context

On 19 October 2012, the day preceding IOP 15a, a high amplitude trough deepened over the north-western part of the Iberian Peninsula (Spain and Portugal) at 500 hPa level; A quasi-stationary cold front extended from eastern Spain to the North Sea (Fig. 3a), bringing warm and moist air masses on the southern slopes of the Pyrenees from the Balearic Sea. Flamant *et al.* (2015) reported that on 19 October the largest 24 h rainfall amounts (in excess of 150 mm) were observed in the Pyrenees, just south of the city of Lourdes (not shown, see their Fig. 2e). Flooding in the area of Lourdes peaked on that day, the Gave de Pau River being 3.50 m above its normal level.

On 20 October, the quasi-stationary cold front continuously extended from north-eastern Spain to Norway (Fig. 3b). A secondary low (1009 hPa) formed over the eastern Spanish coastal region, in the warm area to the east of the quasi-stationary cold front. It develops in the lee (east of) of the Iberian Plateau over the Balearic Sea as commonly observed under similar synoptic situation as a result of interaction of the air flow with orography (Romero *et al.* 2000; Campins *et al.* 2011). This low pressure center induced a cyclonic south-easterly flow between the Balearic Islands and continental Spain. South-easterlies (~10 m s^{-1}) were observed at the surface by radiosondes launched in Palma de Majorca at 0000 and 1200 UTC, while the upper-level flow (~20 m s^{-1}) over eastern Spain was essentially southerly (Fig. 3d).

3.2. Surface precipitation

Intense rainfalls (in excess of 130 mm in 24 h) were recorded over north-eastern Spain on 20 October (Fig. 1). Two long-lived MCSs formed on that day, associated with the secondary low: i) the first one, offshore and south of Valencia around 0720 UTC (hereafter referred to as 'MCS A') as shown in Fig. 2a with the minimum of SEVIRI 10.8 µm BT less than 210 K (cloud top height at ~13 km amsl) and ii) the second one near the coastline in the vicinity of the Ebro River delta around 1300 UTC (hereafter referred to as 'MCS B', Fig. 2c). The temporal evolution of the maximum hourly rainfall (bars in Fig. 1b) recorded by the rain gauge network in the ERV region (i.e. the ERV box in Fig. 1a) shows a first intense rainfall episode of 22 mm h^{-1} occurring between 0900−1000 UTC on 20 October 2012, at a latitude of 40.2°N (grey line, Fig. 1b) corresponding to the time when MCS A was partly observed in the ERV box, as shown in Fig. 2b. With the northward displacement of MCS A between 1000 and 1200 UTC, intense rainfalls (~15 mm h^{-1}, bars in Fig. 1b) were measured at more northern latitudes (grey line in Fig. 1b) within the ERV domain. Subsequently, MCS A travelled northward towards the western Pyrenees guided by the upper-level southerly flow (Fig. 2c). The second intense rainfall period in the ERV box (Fig. 1b) was associated with the presence of MCS B and occurred from 1300 to 1800 UTC, with a maximum rainfall of 28 mm h^{-1}, recorded between 1300−1500 UTC along the foothills of the Iberian Plateau. Between 1300−1800 UTC the northward propagation of MCS B from the north-eastern tip of the Iberian Plateau to the southern Pyrenees is seen in the evolution of AWS location of the maximum hourly rainfall (grey solid line in Fig. 1b). The hourly rainfall measured at station **F** (Foothill, elevation of 500 m amsl, see Fig. 1a) and the neighbouring rain gauge at station **C** (Coast, elevation of 100 m amsl, Fig. 1a) are indicated in Fig. 1b. At station **F** (black solid line), 78 mm of precipitation were accumulated in 3 hours from 1200 UTC, whereas less than one third that amount (25 mm in 3 h; dashed line) were accumulated at station **C**, which is located ~34 km away from station **F**. Later, between1500−1800 UTC, an hourly rainfall of 15 mm h^{-1} was recorded at station **P** (Pyrenees, elevation of 1400 m amsl, Fig. 1a).

The environment leading to the formation of MCS B which brought intense rainfall to the foothill of Iberian Plateau and southern Pyrenees during 1200−1800 UTC is analysed in details thanks to observations and AROME-WMED modelling in the following sections.

4. Pre-convective conditions for MCS B

4.1. Mesoscale low-level conditions

OSCAT-derived surface winds upstream of the initiation region of MCS B around 1300 UTC highlighted three distinct regions with different wind directions (Fig. 4): 1) a region of south-westerly winds (≤ 8 m s^{-1}) west of the Ibiza Island, 2) south-easterly winds (~5 m s^{-1}) from northern Africa to the Balearic Islands that veer to 3) east-south-easterly winds (≥ 10 m s^{-1}) north of Majorca and Minorca. The 10-m wind field from the AROME analysis at 1200 UTC (Fig. 5b) is consistent with the OSCAT one. The AROME-WMED analysis at 1200 UTC (Fig. 5) is used to describe the mesoscale conditions prior to MCS B triggering. The quasi-stationary cold front (broken line in Fig. 5a) over the Iberian Peninsula, south-north elongated along latitude 2°W−1°E, was associated with a significant horizontal gradient of wet-bulb potential temperature at 950 hPa level (Fig. 5a). The secondary low was characterized by a minimum mean sea level pressure (MSLP) below 1009 hPa at 0°E/39.2°N (cross mark in Fig. 5a, c, e), offshore of Valencia. Along the north-eastern flank of the secondary low, a warmer and moister air mass (wet-bulb potential temperature at 950 hPa up to 293 K and 2-m temperature over the sea up to 24−25°C) moving cyclonically around the low was transported northwards, towards the Spanish coast (Fig. 5a, b). The TIWV values of this air mass were very high, between 40−50 kg m^{-2} in the AROME-WMED analysis in agreement with the GPS stations along the coast (Fig. 5c). The GPS-derived hourly TIWVs at 0.3°E, 40.4°N are shown as crosses in Fig. 1b. Very high TIWVs between 38−41 kg m^{-2} were continuously recorded. It is worth noting that during IOP 15a some of the highest GPS-measured TIWV values observed during SOP1 were recorded.

Associated with these large TIWVs and high low-level air temperatures upstream of the ERV region, high convective available potential energy (CAPE) values, larger than 1000 J kg^{-1} (Fig. 5e) were analysed by AROME-WMED from the Balearic Sea to the Ebro River delta region. They are in agreement with the radiosonde measurements at Palma de Mallorca at 1200 UTC which revealed a CAPE value of 938 J kg^{-1} (not shown). The convective inhibition (CIN) in Mallorca at 1200 UTC was on the order of 40 J kg^{-1}, while the CIN at 0600 UTC was on the order of 152 J kg^{-1}. At 1200 UTC, the level of free convection (LFC) and lifting condensation level (LCL) were on the order of 811 and 877 hPa, respectively, and no significant stable layers were observed. It is worth noting that CAPE and TIWV were maximum at 1200 UTC while CIN, LFC, and LCL were minimum at that time, indicating that environmental conditions were most favourable for convective initiation at 1200 UTC.

The vertical structure of the lower layer of the troposphere upstream of the troposphere is shown in Figure 6a and 6b by the vertical cross-section of AROME-WMED analysis of temperature and WVMR along a line A−A’ and a line B−B’ (black lines in Fig. 5b), respectively. Figure 6a evidences the western limit of this warm and moist air mass (hereafter referred to as ‘moisture tongue’) near longitude 1.3°E. Around 1.3°E, very high temperatures from the surface to almost 1000 m amsl were associated to east-south-easterlies transporting this air mass towards the ERV delta. South of this moisture tongue (south of 1.3°E, Fig. 6a), weak south-easterlies (~6 m s^{-1}) with temperature of about 21°C were analysed near the surface; to the north of the moisture tongue (north of 4.2°E), strong easterlies (~13 m s^{-1}) prevailed with temperatures of about 20°C (Fig. 6a). Compared to a similar cross-section at 0900 UTC (not shown), the thickness and maximum temperature of the moisture tongue increased at 1200 UTC. This deepened moisture tongue with higher temperatures appeared to be affected by an enhanced cyclonic circulation associated with the secondary low and the convergence of the southerlies along the eastern flank of the low and the south-easterlies maritime flow in the moisture tongue, upstream of the ERV region. A cross-section of Figure 6b intersects the initiation point of MCS B and is oriented along the low-level south-easterly winds. Point B’ is located over the Balearic Sea between the Islands of Mallorca and Ibiza (see Fig. 5b). High values of WVMRs in excess of 13 g kg^{-1} (contours of Fig. 6b) are seen between 0.5−2.5°E. The deepest moist layer is seen over the Balearic Sea, in the gap between Mallorca and Ibiza, where the 13 g kg^{-1} and 14 g kg^{-1} contours reaches 800 and 600 m amsl, respectively, suggesting reduced stability in that region. Furthermore, the height of the 11, 12, and 13 g kg^{-1} WVMR contours are seen to be significantly higher downstream of the two islands (i.e. between 0.5 and 2°E) than upstream of the gap. This is an indication of more instable condition characterizing the air mass over the western part of the Balearic Sea, before impinging on the coastal range.

4.2. Moisture distribution

Over the Balearic Sea, i.e. upstream of where MCS B developed in the exit region of the ERV, the daily composite of the MODIS-derived moisture (Fig. 7a, acquired around 1230 UTC) shows high values of TIWV between 30−35 kg m^{-2}. About 70% of the TIWV (~24 kg m^{-2}) was distributed between the surface and 700 hPa (not shown). The large TIWV values over the western Mediterranean Sea were observed to be partly associated with an elevated moist plume coming from West Africa as shown by the PIWV composite (values in the range 7−13 kg m^{-2}, Fig. 7b), with most of the moisture (~10 kg m^{-2}) being distributed between 700−600 hPa (not shown). The elongated moist filament from Tropical Africa overpassed the Balearic between 19 and 20 October 2012. On 20 October, the main part moist filament was seen over Corsica and Sardinia (Fig. 7b). Nevertheless high PIWV values are also observed over the Balearic Islands as a result of the circulation, as reported by Chazette *et al*. (2016) for the case of HPE over the Cévennes, southern France, during IOP 15b. The presence of such elevated moist plume was also shown in Lee *et al.* (2016) during IOP 13. The impact of mid-level moisture transport on the development and maintenance of HPEs has been demonstrated in other regions of the world, as the entrainment of moist mid-level air (around 3−4 km amsl) leads to an increase in precipitable water vapour column available for orographic rainfall (Kaplan *et al.* 2009). In our case, this mid-level plume appears to affect areas further eastward than the region of MCS B triggering.

The ATR 42 aircraft flew upstream the ERV region. More details on the vertical structure of the low-level moisture field upstream region of the ERV region where MCS B was initiated are provided by LEANDRE 2-derived WVMR observations between 1100 and 1300 UTC. Figures 8a displays LEANDRE 2 observations between 1050 UTC and 1140 UTC along the blue solid line in Fig. 1a. The ATR 42 flight track crossed over the moisture tongue in Figure 8a south of about 40°N.

In Fig. 8a, a very moist layer is observed near the surface with WVMRs in excess of 14 g kg^{-1}. When approaching the moisture tongue, the depth of this very moist layer was observed to decrease significantly to about 100 m as the mixing above increase. Above this moist layer, LEANDRE 2 observations evidenced a drier air mass in the northern part of the leg (41.5−40°N) with WVMRs on the order of 5−6 g kg^{-1} below 2 km amsl and moister air masses in the moisture tongue in the southern part of the leg (40−39°N) characterized by WVMRs between 10 and 14 g kg^{-1}. Some low-level clouds at the flight level ~2.6 km amsl of the ATR42 can be seen in the LEANDRE 2 observations in the vicinity of the Ibiza Island in the southernmost part of the leg.

The high low-level moisture values and moisture feature observed with LEANDRE 2 (Fig. 8a) are correctly represented in AROME-WMED analyses. Figure 8b displays AROME-WMED WVMR profiles extracted from the 1200 UTC analysis at the closest location in space to the LEANDRE 2 WVMR profiles. A satisfactory agreement is found between the AROME-WMED analysis and LEANDRE 2 observations north of 40°N (Fig. 8b), both in terms of the moisture structures and content (see also Fig. 8c). Even if AROME-WMED low-level moisture north of 41° extends too high, the AROME-WMED analysis captures the decrease of the depth of the moist surface layer and concomitant increase of the mixing above. Figure 8c highlights that the gradient at the top of the MABL is not well reproduced by AROME (AROME biased high by 2 g kg^{-1} on average at 600 m amsl) and that difference can exceed −3 g kg^{-1}. Above 900 m amsl, the mean difference between LEANDRE 2 and AROME is much reduced (±0.5 g kg^{-1}) with AROME biased low. It is also worth noting that the standard deviation associated with the difference between the observations and the model is ~2 g kg^{-1} throughout the lower troposphere. This is mostly due to the fact that numerous small scale structures are observed in the moisture field derived from LEANDRE 2 that are not present in the AROME field.

The high low-level moisture values observed with LEANDRE 2 and analysed by AROME-WMED are known to be one of the main ingredients of the mesoscale environment enabling heavy precipitation.

5. MCS B Initiation

5.1. Low-level winds in the MCS B triggering region

At the foothill of the Iberian Plateau (0.25−0.75°E, 40.5−41°N), strong convergence (6×10^{-4} s^{-1}) between maritime east-south-easterlies (10 m s^{-1}) and weak inland north-westerlies (3 m s^{-1}) blowing down the ERV region and along the Iberian Plateau was analysed by AROME-WMED (Fig. 5d) and observed by AWS station (Fig. 5e). North-westerly winds (4.2 $m s^{-1}$; Fig. 5e) were observed at the north-easternmost AWS station (marked as ‘e’ in Fig 2b, altitude ~300 m amsl), while very weak easterlies (~1 $m s^{-1}$) were seen at the location of the gap between the Iberian Plateau and the Catalan mountain range (marked as ‘d’ in Fig. 2b, altitude ~100 m amsl), evidencing the strong near-surface wind convergence upstream of the convection initiation area. At station ‘e’, the north-westerlies were persistently measured during all the day, while very weak easterlies to south-easterlies were seen constantly at the station ‘d’ during 0900−1500 UTC; the terrain-induced wind convergence at the foothill of the Iberian Plateau was stationary during that time. The two southernmost stations (marked as ‘a’ and ‘b’) on the coast were influenced by the surface low located to the south of Valencia (Fig. 5e), showing the north-easterlies, while easterlies were seen at the easternmost station (marked as ‘c’ in Fig. 2b).

5.2. MCS B triggering

Around 1200 UTC, a convective line within the cloud cluster was identified by large ground-based radar reflectivities (in excess of 30 dBZ, Fig. 9d) from the mainland Spanish coast to the north of Ibiza. It was associated with the convergence between the low-level cooler south-westerly winds and the warmer south-easterly winds (near 0.3°E in Fig. 6a) along the north-eastern flank of the secondary low (Fig. 5a, b). Lightning associated with the convective line first occurred at the coast around 1300 UTC (Fig. 9b), suggesting enhanced convection at the northern tip of the convective line. MCS B initiation took place over the south-western slopes (terrain height of 500−1000 m) of the ERV exit (~0.5°E/40.8°N, where terrain elevation can reach 1200 m amsl) as indicated by the colder cloud top just north-east of the convective line in the 10.8 μm BTs at 1300 UTC (Fig. 9b). MCS B triggering occurred in the terrain-induced convergence area (Fig. 5d), with north-westerly wind channeled in the ERV and encountering marine warm easterly winds. The convective line observed by radar (Fig. 9d−e) progressed north-westward from 1230 UTC to 1300 UTC and merged with MCS B when it crossed the elevated terrain south-west of the ERV exit gap near 1330 UTC (Fig. 9f), where MCS B was previously initiated. This suggests that the convergence line itself was not solely responsible for triggering MCS B, and that additional possibly orographic forcing was needed in order for embedded deep convection to be triggered on the north-easternmost tip of the Iberian Plateau.

6. MCS B development

From 1400 UTC, MCS B moved from the foothill of the Iberian Plateau (Fig. 10), northward, across the ERV, towards the Central Pyrenees, as shown by the progression of the low BT ≤ 210 K (cloud top height ~13 km amsl, not shown) between Fig. 10a and Fig. 10c. Within the low BT area characterizing MCS B, reflectivity was on the order of 30−35 dBZ, but higher reflectivity, in excess of 40 dBZ, was observed near the mountain foothill during 1400−1500 UTC (Fig. 10d−e).

From 1435 UTC to 1450 UTC, the F20 flew along the southern side of MCS B (red/black line in Fig. 10b and 10e) from its anvil south of the Pyrenees (mark **S** with white circle) to its apex north of the foothill of Iberian Plateau (white star). The observed vertical profiles of reflectivity and vertical wind component derived from the cloud radar RASTA are shown in Fig. 11.

The RASTA reflectivity field (Fig. 11a) shows the structure of a well-developed MCS with three distinct regions with different vertical reflectivity profiles. First, at the apex of MCS B, a quite patchy region of high reflectivity (≥ 10 dBZ) from ~3.5 km to 13 km amsl, typical of convective clouds is observed, adjacent to the foothill of the Iberian Plateau (41.1−40.9°N; 1447−1450 UTC). Maximum reflectivity (~18 dBZ) is reached between 4 and 8 km amsl. Then a region with high reflectivity (≥ 10 dBZ) from 4.5 km to 12 km amsl, with a bright band below at ~3.5 km amsl over the ERV area (41.5−41.2°N; 1441−1445 UTC). Finally, a structure of slanted high-level high reflectivities indicating an anvil cloud region with a bright band below is observed near the southern foothill of Pyrenees (41.8−41.5°N; 1435−1440 UTC). In the first region, at the apex of MCS B, intense updrafts over 2 m s^{-1} were observed from 4 km to 12.5 km amsl, and even more intense updraft exceeding 7 m s^{-1} were observed between 7 and 10 km amsl (Fig. 11b). In the second reflectivity region, moderate updrafts of 1−3 m s^{-1} are shown in 6−13 km amsl, while the anvil cloud region was mostly showing weak downdrafts of −1.5 m s^{-1}. The observed bright band phenomena between 3 km and 4 km amsl with locally increased reflectivities, is a melting layer (Fig. 11a). Due to the presence in a mixture of liquid and ice medium, the reflectivity was increased locally by the change in refractivity index. Below the melting layer (temperature > 0°C), precipitation mostly consists of rain, and is not properly sampled by the cloud radar due to attenuation by liquid precipitation at high frequencies (95 GHz).

A very moist and warm air mass was conveyed towards the strongest convective updrafts with high temperatures (wet-bulb potential temperature at 950 hPa up to 293 K and 2-m temperature higher than 22°C) near the Catalan coast (Fig. 12a, b) and with TIWVs in excess of 40 kg m^{-2} at the ERV exit region (Fig. 12c). These features are well reproduced in the AROME-WMED analysis at 1500 UTC. As the secondary low moved further north-eastward and the easterly winds approached Barcelona (Fig. 12b, d), the wind at the southernmost station (Fig. 12d) shifted from north-easterly to southerly, and the moisture tongue upstream of the ERV became narrower (Figs. 12b) when compared to previous periods (i.e. Figs. 5b). Associated with this warm and moist air, AROME-WMED simulates CAPE in excess of 900 J kg^{-1}, spanning from the Majorca Island to the Catalan coastline (Fig. 12e). Offshore of the Catalan coastal range, north of the low MSLP (~1008 hPa, cross in Fig. 12e), southerlies (8 ms^{-1}) and easterlies (5 ms^{-1}) further north merged creating a convergence in excess of 5×10^{-4} s^{-1} in the ERV exit region; at the foothill of the Iberian Plateau near the narrowest orographic gap, the terrain-induced stationary wind convergence of north-westerlies, south-easterlies and easterlies could be observed (Fig. 12d, e), corresponding to the location of the strongest convective updrafts observed with the RASTA radar.

After 1600 UTC (Fig. 10c and 10f), MCS B moved toward the central Pyrenees, exhibiting a wide-spread anvil in the BT imagery (≤ 210 K) and radar reflectivity (≥ 30 dBZ). The system became less active with less reflectivity over 40 dBZ (Fig. 10f). MCS B eventually dissipated over the Pyrenees in the evening (now shown).

7. Summary

During IOP 15a (20 October 2012) of the HyMeX SOP 1, the mountainous region of north-eastern Spain and the **ERV** region (box in Fig. 1a) experienced intense rainfalls (in excess of 130 mm in 24 h) under the combined influence of an approaching upper-level trough and a secondary surface low moving north-eastward along the coastal mountain range (Iberian Plateau and Catalonia). In this synoptic situation, a flow regime with south-easterlies in low levels and southerlies in the mid-levels was generated upstream of the ERV. Associated with this synoptic flow regime, two MCSs developed near the coastal mountain region of the Iberian Plateau that brought intense rainfall over the ERV region. In this study, the second MCS forming during IOP 15a was targeted by HyMeX dedicated observational airborne platforms. The characteristics of the marine south-easterly flow and the dynamical ingredients upstream in connection with the life cycle of MCS were investigated through a detailed analysis using an unprecedented wealth of data, including measurements from two aircraft, standard observational networks and the analyses of a numerical weather prediction model. To the authors knowledge, only very few previous field experiments have aimed at describing the moisture field in pre-convective conditions, among which the International H2O project (Weckwerth *et al.*, 2004) and the Convective and Orographically Induced Precipitation Study (Wulfmeyer *et al.*, 2011).

The main findings are summarized in schematic illustrations shown Fig. 13. Over the Balearic Sea upstream of the ERV region, the south-westerly winds progressively veering to south-easterly winds along the north-eastern flank of the secondary low (marked **D** in Fig. 13) transported a warm and moist converging air mass towards the Spanish coast. Airborne lidar measurements upstream of the ERV exit region and across the moisture tongue along the north-eastern flank of the low, evidenced the very moist low-level flow with WVMRs in excess of 15 g kg^{-1} near the surface and WVMRs as high as 13−14 g kg^{-1} between 1 and 2 km amsl, in connection with the large cloud cluster band extending from North Africa and the south-easterly flow. Moreover, the mid-level flow (700 hPa) was enriched by the presence of an elevated moisture plume from tropical Africa which contributed for about one third to the large moisture content (TIWV ~35 kg m^{-2}) over the western Mediterranean Sea. The presence of an elevated moisture plume from tropical Africa was also observed during other HPEs during HyMeX SOP1, e.g. HPE in Southern Italy during IOP 13 (Lee *et al.* 2016) and HPE in the Cevennes-Vivarais of Southern France during IOP 15b (Chazette *et al.* 2016). This suggests that the presence of a north-south elongated upper-level trough appears to be crucial for advecting mid-level moisture plumes from tropical Africa to Western Europe.

In this environment, MCS B was initiated over the eastern tip of the Iberian Plateau (Fig. 13a), where terrain elevation can reach 1200 m amsl, and is higher than the surrounding terrain. MCS B triggering occurred in the terrain-induced convergence area between the marine moist and conditionally unstable low-level easterly winds impinging on the coastal range and weaker north-westerly wind channelled in the ERV region. MCS B very rapidly merged with the convective line associated with the convergence in the low-level south-westerly to south-easterly winds ahead of the secondary low. The convergence between the weak north-westerlies channelled in the ERV and the easterlies impinging on the coastal range was present from early morning on, but yet no MCS was triggered. Likewise the convergence line ahead of the surface low progressed north-eastward, across the coastal range for some time before reaching the ERV exit region and was associated only with weak convective activity. This suggests that the low-level convergence was not solely responsible for triggering MCS B, and that additional orographic forcing was needed in order for embedded deep convective to be triggered on the north-easternmost tip of the Iberian Plateau. After the initiation phase, MCS B further developed over the foothill of Iberian Plateau into the ERV and along the southern flanks of the Pyrenees, thanks to the penetration of the warm and moist south-easterly maritime flow through, the narrow gap between the north-eastern part of the Iberian Plateau, and the Catalan coastal range (Fig. 13b).

This study highlights how local orography features, mesoscale low-level circulation and large-scale synoptic forcing interplay to produce peculiar MCSs embedded in a large scale disturbances resulting in high precipitation rates locally. Many previous studies on HPEs occurring around north-eastern Spain (Romero *et al*. 1999; Sotillo *et al*. 2003; Trapero *et al.* 2013a, 2013b) revealed that low pressure centers located over the Iberian Peninsula lead to a favourable environment for MCS development over the eastern/northern parts of Pyrenees. In this study, the upper-level trough and the associated southerly flow from the Tropics to Western Europe, together with the development of a secondary surface low located east of the Iberian Plateau, provided the favourable environment for the development of MCSs south of the Pyrenees during IOP 15a. The location of the surface low at the north-eastern coast of Iberian Peninsula and its north-eastward displacement played an important role in generating the near surface tongue of warm and moist air in the upstream region of the ERV which supplied the south-easterly maritime flow to the ERV region. Within this favourable environment, convection is triggered by the orography of the Iberian Plateau associated with both small-scale low-level orographically-induced convergence areas and convergence ahead of the secondary surface low. Moreover, in this study, we provide insights into the very moist marine environment over the Balearic Sea (i.e. TIWV in excess of 30 kg m^{-2}), upstream of MCSs convective initiation region, using airborne observations never acquired before in this data-scarce environment. The spatial distribution of moisture, was highlighted using a unique combination of ground-based (GPS, radiosondes), airborne (lidar) and space-borne (MODIS) observations.

Appendix

The used acronyms are listed in Table 1.

Acknowledgement

This work was supported by the French Agence Nationale de la Recherche (ANR) via the IODA-MED Grant ANR-11-BS56-0005, the MUSIC grant ANR-14-CE01-014, the MISTRALS/HyMeX programme and the Spanish project CGL2015-65627-C3-2-R (MINECO/FEDER). Airborne data was obtained using the ATR-42 Environment Research Aircraft operated and managed by Service des Avions Français Instrumentés pour la Recherche en Environnement (SAFIRE), which is a joint entity of CNRS, Météo-France & CNES. The SAFIRE staff is thanked for their support during the SOP 1. Authors are grateful to O. Bock of LAREG-IGN, Université Paris Diderot for providing GPS network data, and to D. Bruneau, P. Genau, C. Merlet, R. Meynadier, T. Deleporte, S. Bastin, C. Kocha, C. Lavaysse (LATMOS) as well as F. Blouzon and A. Abchiche (DT/INSU) for operating the LEANDRE 2 system aboard the ATR-42 during the HyMeX-SOP 1.

Finally, the authors are grateful to the three anonymous referees whose comments helped improved the paper significantly.

LEANDRE 2 data are available from the HyMeX Database: http://dx.doi.org/10.6096/MISTRALS-HYMEX.WATER_VAPOUR_DIAL_LEANDRE2.V1.20120911. AROME-WMED analyses are also available from HyMeX database: http://dx.doi.org/10.6096/HYMEX.AROME_WMED.2012.02.20.

References

Bedka KM. 2011. Overshooting cloud top detections using MSG SEVIRI Infrared brightness temperatures and their relationship to severe weather over Europe. *Atmos. Res.* **99**: 175−189, doi: 10.1016/j. atmosres.2010.10.001.

Bock O, Bosser P, Pacione R, Nuret M, Fourrié N, Parracho A. 2016. A high quality reprocessed ground-based GPS dataset for atmospheric process studies, radiosonde and model evaluation, and reanalysis of HyMeX special observing period. *Q. J. R. Meteorol. Soc.* **142**: 56−71, doi :10.1001/qj.2701.

Bouniol D, Protat A, Plana-Fattori A, Giraud M, Vinson JP, Grand N. 2008. Comparison of airborne and spaceborne 95 GHz radar reflectivities and evaluation of multiple scaterring effects in spaceborne measurements. *J. Atmos. Oceanic Technol.* **25**: 1983−1995, doi: 10.1175/2008JTECHA1011.1.

Bousquet O, Delanoë J, Bielli S. 2016. Evalution of 3D wind observations inferred from the analysis of airborne and ground-based radars during HyMeX SOP-1. Q. J. R. Meteorol. Soc. **142**: 86−94 doi: 10.1002/qj.2710.

Bousquet O, Smull BF. 2006. Observed mass transports accompanying upstream orographic blocking during MAP IOP8. *Q. J. R. Meteorol. Soc*. **132**: 2393−2413.

Brousseau P, Bouttier F, Hello G, Seity Y, Fischer C, Berre L, Montmerle T, Auger L, Malardel S. 2008. A prototype convective-scale data assimilation system for operation: The AROME-RUC. HIRLAM Tech. Rep. 68: 23−30.

Bruneau D, Quaglia P, Flamant C, Meissonnier M, Pelon J. 2001a. Airborne Lidar LEANDRE 2 for water vapour profiling in the Troposphere. System description. *Appl. Opt*. **40**: 3450−3461.

Bruneau D, Quaglia P, Flamant C, Pelon J. 2001b. Airborne Lidar LEANDRE 2 for water vapour profiling in the Troposphere. First results. *Appl. Opt*. **40**: 3462−3475.

Campins J, Genovés A, Picornell MA, Jansà A. 2011. Climatology of Mediterranean cyclones using the ERA-40 dataset. *Int. J. Climatol.* **31**: 1596−1614, doi: 10.1002/joc.2183.

Chazette P, Flamant C, Raut JC, Totems J, Shang X. 2016. Tropical moisture enriched storm tracks over the Mediterranean and their link with intense rainfall in the Cevennes-Vivarais area during HyMeX. *Q. J. R. Meteorol. Soc*. **142**: 320−334, doi:10.1002/qj.2674.

Courtier P, Freydier C, Geleyn JF, Rabier F, Rochas M. 1991. The ARPEGE project at Meteo-France, ECMWF workshop on numerical methods in atmospheric modeling, **2**: 193–231.

Delanoë JME, Protat A, Jourdan O, Pelon J, Papazzoni M, Dupuy R, Gayet JF, Jouan C. 2013. Comparison of airborne in situ, airborne radar-lidar, and spaceborne radar-lidar retrievals of polar ice cloud properties sampled during the POLARCAT campaign. *J. Atmos. Oceanic Technol*. **30**: 57−73, doi: 10.1175/JTECH-D-11-00200.1.

Di Girolamo P, Flamant C, Cacciani M, Richard E, Ducrocq V, Summa D, Stelitano D, Fourrié N, Said F. 2016. Observation of low-level wind reversals in the Gulf of Lion area and their impact on the water vapour variability, *Q. J. R. Meteorol. Soc*. **142**: 153−172, doi:10.1002/qj.2767.

Ducrocq V, Braud I, Davolio S, Ferretti R, Flamant C, Jansa A, Kalthoff N, Richard E, Taupier-Letage I, Ayral PA, Belamari S, Berne A, Borga M, Boudevillain B, Bock O, Boichard JL, Bouin MN, Bousquet O, Bouvier C, Chiggiato J, Ciimini D, Corsmeier U, Coppola L, Cocquerez P, Defer E, Delanoë J, Di Girolamo P, Doerenbecher A, Drobinski P, Dufournet Y, Fourrié N, Gourley JJ, Labatut L, Lambert D, Le Coz J, Marzano FS, Molinié G, Montani A, Nord G, Nuret M, Ramage K, Rison W, Roussot O, Said F, Schwarzenboeck A, Testor P, Van Baelen J, Vincendon B, Aran M, Tamayo J. 2014. HyMeX-SOP1: The Field Campaign Dedicated to Heavy Precipitation and Flash Flooding in the Northwestern Mediterranean. *Bull. Am. Meteorol. Soc.* **95**: 1083−1100, doi:10.1175/BAMS-D-12-00244.1.

Duffourg F, Nuissier O, Ducrocq V, Flamant C, Chazette P, Delanoë J, Doerenbecher A, Fourrié N, Girolamo Di P, Lac C, Legain D, Martinet M, Saïd F, Bock O. 2016. Offshore deep convection initiation and maintenance during HyMeX IOP 16a heavy precipitation event. *Q. J. R. Meteorol. Soc.* **142**: 259−274, doi:10.1002/qj.2725.

Duffourg F, Ducrocq V. 2013. Assessment of the water supply to Mediterranean heavy precipitation: A method based on finely designed water budgets. *Atmos. Sci. Lett.* **14**: 133−138.

Flamant C, Chaboureau JP, Chazette P, Di Girolamo P, Bourianne T, Totems J, Cacciani M. 2015. The radiative impact of desert dust on orographc rain in the Cevennes-Vivarais area: a case study from HyMeX. *Atmos. Chem Phys.* **15**: 12231−12249.

Flaounas E, Kotroni V, Lagouvardos K, Claud C, Delanoë J, Flamant C, Madonna E, Wernli H. 2016. Processes leading to heavy precipitation associated with two Mediterranean cyclones observed during the HyMeX SOP1. *Q. J. R. Meteorol. Soc.* **142**: 275−286, doi:10.1002/qj.2618.

Fourrié N, Bresson E, Nuret M, Jany C, Brousseau P, Doerenbecher A, Kreitz M, Nuissier O, Sevault E, Bénichou H, Amodei M, Pouponneau F. 2015. Arome-wmed, a real-time mesoscale model designed for the HyMeX special observation periods. *Geosci. Model Dev.* **8**(**2**): 1801−1856, doi:10.5194:/gmdd-8-1801-2015.

Kaplan, M. L., C. S. Adaniya, P. J. Marzette, K. C. King, S. J. Underwood, and J. M. Lewis, 2009. The Role of Upstream Midtropospheric Circulations in the Sierra Nevada Enabling Leeside (Spillover) Precipitation. Part II: A Secondary Atmospheric River Accompanying a Midlevel Jet. *J. Hydrometeor.*, **10**, 1327−1354, doi:10.1175/2009JHM1106.1.

Kato T. 2006. Structure of the band-shaped precipitation system inducing the heavy rainfall observed over northern Kyushu, Japan on 29 June 1999. *J. Meteor. Soc. Japan*. **84**(**1**): 129−153.

Lee KO, Flamant C, Ducrocq V, Duffourg F, Fourrié N, Davolio S. 2016. Convective initiation and maintenance processes of two back-building mesoscale convective systems leading to heavy precipitation events in Southern Italy during HyMeX IOP 13. *Q. J. R. Meteorol. Soc.* doi: 10.1002/qj.2851.

Lee KO, Uyeda H, Shimizu S, Lee DI. 2012. Dual-Doppler radar analysis of the enhancement of a precipitation system on the northern side of Mt. Halla, Jeju Island, Korea on 6 July 2007. *Atmos. Res.* **118**: 133−152.

Llasat MC, Llasat-Botija M, Petrucci O, Pasqua AA, Rosselló J, Vinet F, Boissier L. 2013. Towards a database on societal impact of mediterranean floods within the framework of the HyMeX project. *Nat. Hazard Earth Sys.* **13**(**5**): 1337−1350, doi:10.5194/nhess-13-1337-2013.

Li L, Heymsfield GM, Tian L, Racette PE. 2005. Measurements of ocean surface backscattering using an airborne 94-ghz cloud radar‒Implication for calibration of air-borne and space borne W-band radars. *Journal of Atmospheric and Oceanic Technology*. **22**: 1033−1045.

Lorente J, Redaño A. 1990. Rainfall rate distribution in a local scale: the case of Barcelona city. *Teor. Appl. Climatol.* **41**: 23−32.

Mc Cann DW. 1983. The enhanced-V: a satellite observable severe storm signature. *Mon. Wea. Rev*. **111**: 887−894.

Melani S, Pasi F, Gozzini B, Ortolani A. 2013. A four year (2007‒2010) analysis of long-lasting deep convective systems in the Mediterranean basin. *Atmos. Res.*, **123**: 151−166.

Nuissier O, Ducrocq V, Ricard D, Lebeaupin C, Anquetin S. 2008. A numerical study of three catastrophic precipitating events over southern France. I: Numerical framework and synoptic ingredients. *Q. J. R. Meteorol. Soc.* **134**: 111−130.

Nuissier O, Joly B, Joly A, Ducrocq V, Arbogast P. 2011. A statistical downscaling to identify the Large-Scale circulation patterns associated with heavy precipitation events over southern France. *Q. J. R. Meteorol. Soc.* **137(660)**: 1812−1827, doi: 10.1002/qj.866.

Pineda N, Bech J, Rigo T, Montanyà. 2011. A Mediterranean nocturnal heavy rainfall and tornadic event. Part II: Total lightning analysis. *Atmos. Res.* **100**: 638−648.

Protat A, Pelon J, Testud N, Grand P, Delville P, Laborie JP. Vinson D, Bouniol D, Bruneau D, Chepfer H, Delanoë J, Haeffelin M, Noël V and Tinel C. 2004. Le projet RALI: Combinaison d'un radar nauge et d'un lidar pour l'étude des nauges faiblement précipitants. La Météorologie. 8[e] série, n°47: 23−33.

Protat A, Bouniol D, Delanoë J, May PT, Plana-Fattori A, Hasson A, O'Connor E, Görsdorf U, Heymsfield AJ. 2009. Assessment of Cloudsat reflectivity measurements and iced cloud properties using ground-based and airborne cloud radar observations. *J. Atmos. Oceanic Technol.* **26**: 1717−1741, doi: 10.1175/2009JTECHA1246.1.

Ricard D, Ducrocq V, Auger L. 2012. A climatology of the mesoscale environment associated with heavily precipitating events over a northwestern mediterranean area. *J. Appl. Meteorol. Climatol.* **51**: 468−488, doi:10.1175/JAMC-D-11-017.1.

Romero R, Doswell III CA, Ramis C. 2000. Mesoscale numerical study of two cases of long-lived quasi-stationary convective systems over eastern Spain. *Mon. Wea. Rev.* **128**: 3731−3751.

Romero R, Sumner G, Ramis C, Genoves A. 1999. A classification of the atmospheric circulation patterns producing significant daily rainfall in the Spanish Mediterranean area. *Int. J. Climatol.* **19**: 765−785.

Rotunno R, Houze RA. 2007. Lessons on orographic precipitation from the Mesoscale Alpine Programme. *Q. J. R. Meteorol. Soc*. **133**: 811−830.

Seity Y, Brousseau P, Malardel S, Hello G, Bernard P, Bouttier F, Lac C, Masson V. 2011. The AROME-France convective-scale operational model. *Mon. Wea. Rev.* **139**: 976−991, doi:10.1175.2011MWR3425.1.

Sotillo MG, Ramis C, Romero R, Alonso S, Homar V. 2003. Role of orography in the spatial distribution of precipitation over the Spanish Mediterranean zone. *Clim. Res*. **23**: 247−261.

Tanelli S, Durden SL, Im E, Pak KS, Reinke DG, Partain P, Haynes JM, Marchand RT. 2008. Cloudsat's cloud profiling radar after 2 years in orbit: Performance, external calibration, and processing. *IEEE Trans. Geosci. Remote Sens.* **46**: 3560−3573.

Trapero L, Bech J, Lorente J. 2013a. Numerical modelling of heavy precipitation events over Eastern Pyrenees: Analysis of orographic effects. *Atmos. Res*. **123**: 368−383.

Trapero L, Bech J, Duffourg F, Esteban P, Lorente J. 2013b. Mesoscale numerical analysis of the historical November 1982 heavy precipitation event over Andorra (Eastern Pyrenees). *Nat. Hazards Earth Syst. Sci.* **13**: 2969−2990.

Turato B, Reale O, Siccardi F. 2004. Water vapor sources of the October 2000 Piedmont Flood. *J. Hydrometeorol.* **5**: 693−712, doi:10.1175/1525-7541(2004)005<0693:WVSOTO>2.0.CO;2.

Weckwerth T, Parsons D, Koch S, Moore J, Lemone P, Demoz B, Flamant C, Geerts B, Wang J, Feltz W. 2004. An Overview of the International H2O Project (IHOP_2002) and Some Preliminary Highlights, *Bull. Amer. Meteorol. Soc.* **85**, 253−277.

Winschall A, Pfahl S, Sodemann H, Wernli H. 2012. Impact of north Atlantic evaporation hot spots on southern Alpine heavy precipitation events. *Q. J. R. Meteorol. Soc.* **138**: 1245−1258, doi:10.1002/qj.987.

Wulfmeyer V, Behrendt A, Kottmeier C, Corsmeier U, Barthlott C, Craig GC, Hagen M, Althausen D, Aoshima F, Arpagaus M, Bauer HS, Bennett L, Blyth A, Brandau C, Champollion C, Crewell S, Dick G, Di Girolamo P, Dorninger M, Dufournet Y, Eigenmann R, Engelmann R, Flamant C, Foken T, Gorgas T, Grzeschik M, Handwerker J, Hauck C, Höller H, Junkermann W, Kalthoff N, Kiemle C, Klink S, König M, Krauss L, Long CN, Madonna F, Mobbs S, Neininger B, Pal S, Peters G, Pigeon G, Richard E, Rotach MW, Russchenberg H, Schwitalla T, Smith V, Steinacker R, Trentmann J, Turner DD, van Baelen J, Vogt S, Volkert H, Weckwerth T, Wernli H, Wieser A, Wirth M. 2011: The Convective and Orographically Induced Precipitation Study (COPS): The Scientific Strategy, the Field Phase, and First Highlights , *Q. J. R. Meteorol. Soc*. **137**(S1), 3−30.

Table 1. List of the used acronyms.

AROME-WMED	Operational convective-scale Application of Research to Operations at Mesoscale-West Mediterranean Sea
AWS	Automated Weather Station
BT	Brightness Temperature
CAPE	Convective Available Potential Energy
CIN	Convective INhibition
ERV	Ebro River Valley
F20	Falcon 20
GPS	Global Positioning System
HPE	Heavy Precipitation Event
HyMeX	Hydrological cycle in the Mediterranean Experiment
IOP	Intensive Observation Period
MCS	Mesoscale Convective System
MODIS	Moderate Resolution Imaging Spectro-radiometer
MSG	Meteosat Second Generation satellite
OSCAT	Oceansat-2 scatterometer
PIWV	Partial Integrated Water Vapour
RMSE	Root Mean Square Error
LCL	Lifting Condensation Level
LFC	Level of Free Convection
SEVIRI	Spinning Enhanced Visible and Infrared Imager
SOP	Special Observation Period
TIWV	Total Integrated Water Vapour
WVMR	Water Vapour Mixing Ratio

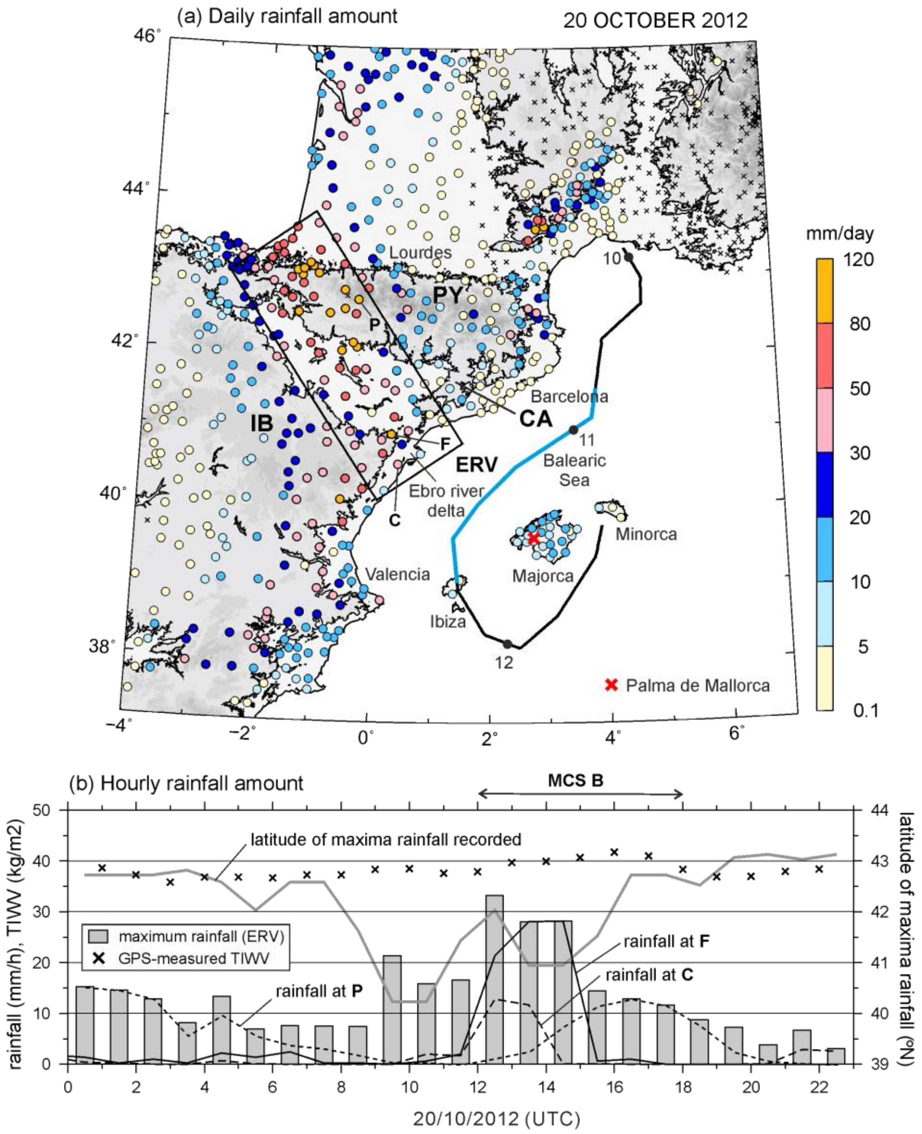

Figure 1. (a) Daily rainfall accumulation (mm) observed on 20 Oct. 2012. The Ebro River Valley (ERV) domain is shown by the solid box. Coastal line and terrain height of 500 m are depicted by thin solid line, and higher terrain is grey-shaded. The trajectory of the ATR42 flight over the Sea is shown as a solid line, with dots indicating the location of the ATR42 every hour, at 1000, 1100 and 1200 UTC. LEANDRE 2 WVMR profiles observed along the blue line are displayed in Fig. 8. (b) Time series of maximum rainfall (bar) within the domain **ERV**, its location (grey solid line: latitude, °N), GPS-measured hourly TIWV (crosses: GPS station at 0.3°E, 40.4°N), hourly rainfalls measured at stations **F** (foothill, black solid line: for rain gauge at 0.3°E, 40.9°N, 0.5 km height), and **C** (coast, dashed line: rain gauge at 0.4°E, 40.6°N, 0.1 km height), and **P** (Pyrenees, dotted line: rain gauge at −0.1°E, 42.7°N, 1.4 km height). In (a), labels **PY**, **CA**, and **IB** mark the topography surrounding the **ERV:** the Pyrenees, the Catalan coastal range, and the Iberian Plateau, respectively.

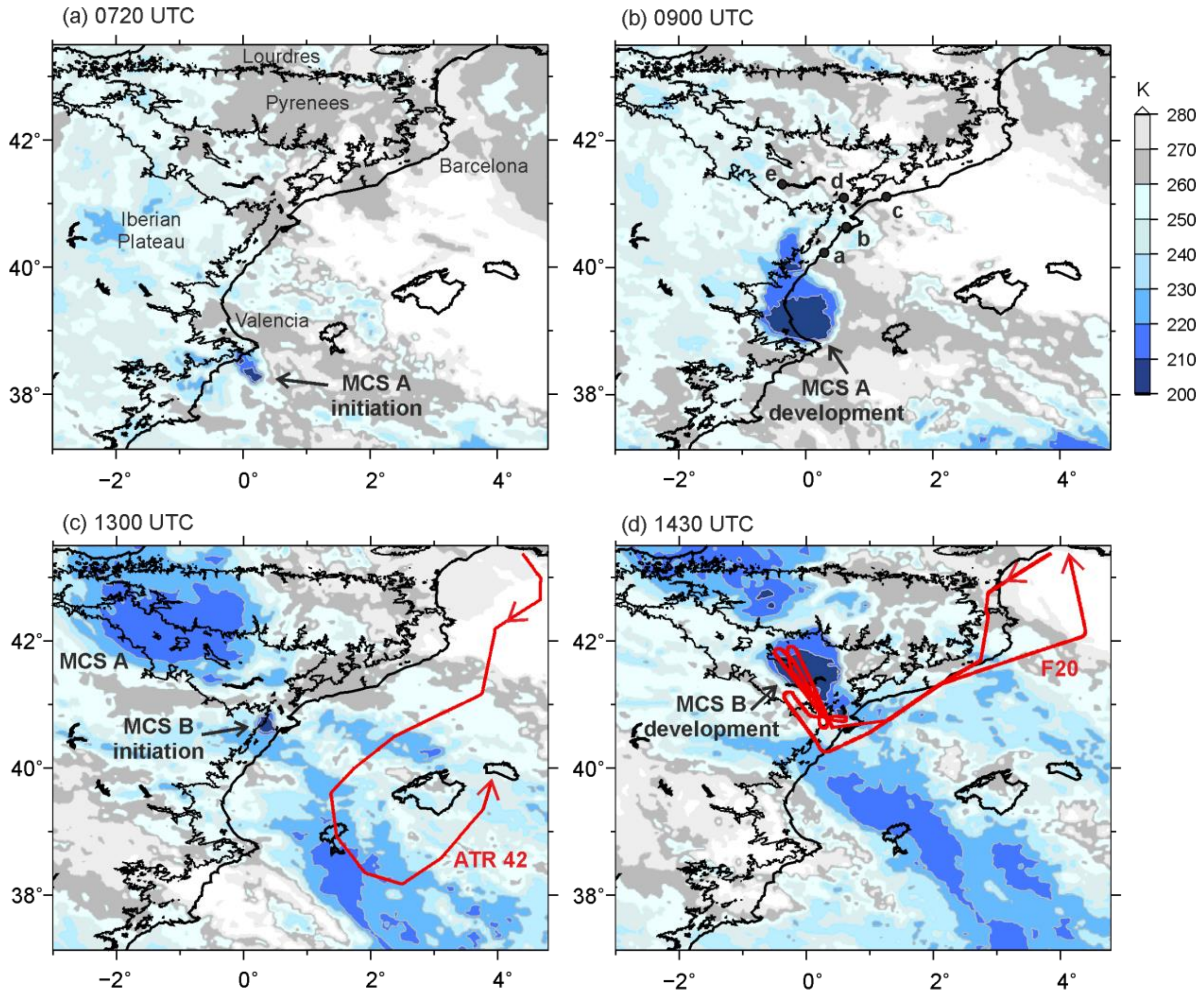

Figure 2. Brightness temperature at 10.8 μm (K) from SEVIRI-MSG at (a) 0720 UTC, (b) 0900 UTC, (c) 1300 UTC, and (d) 1430 UTC on 20 October 2012. The coastal line and the 500 m terrain height are contoured. In (b), the locations of the 5 selected AWS stations are marked by black dots. In (c), the track of the ATR42 aircraft (from 0954 UTC to 1256 UTC) is shown as the red solid line. In (d), the track of the F20 aircraft (from 1320 UTC to 1630 UTC) is shown as the red solid line in (d).

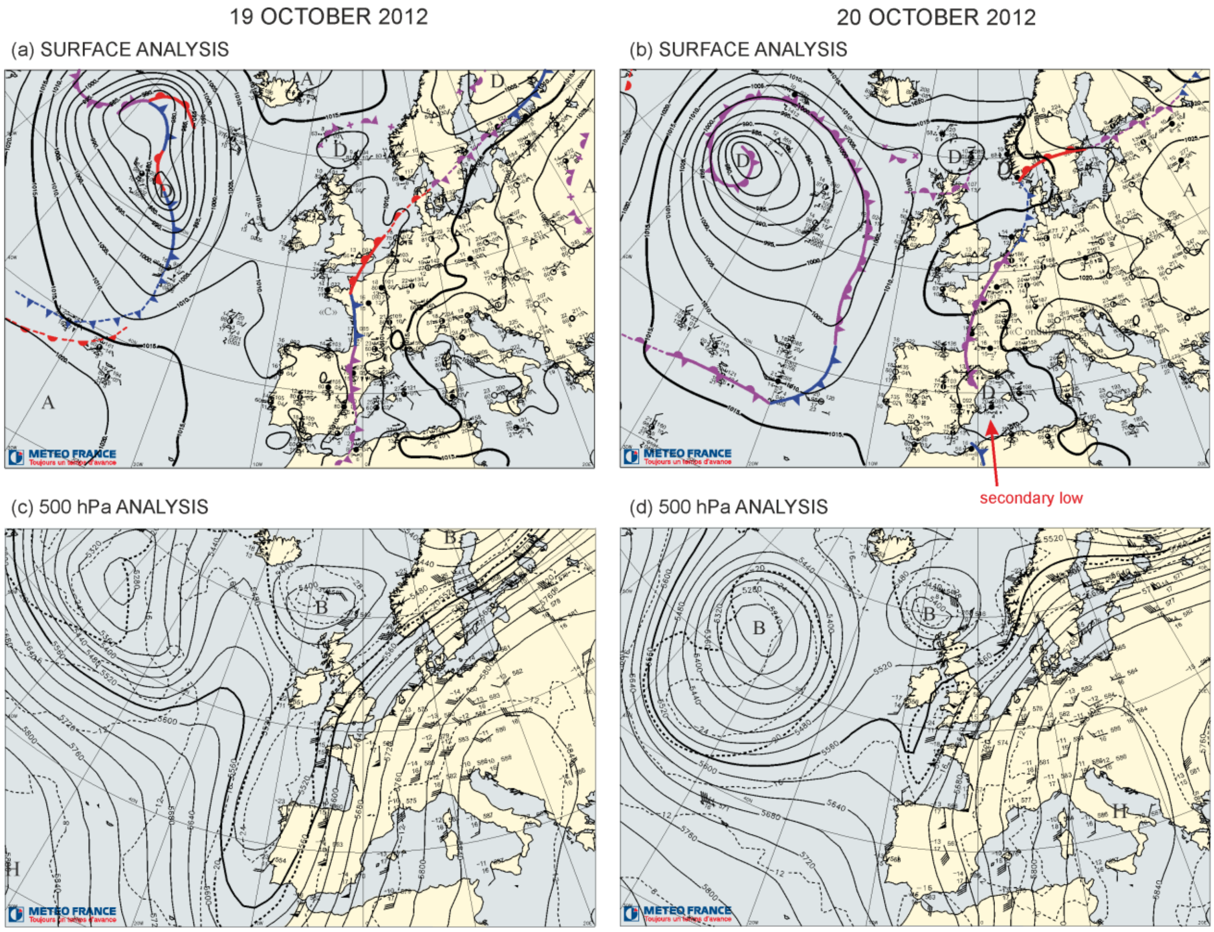

Figure 3. Weather charts at 1200 UTC, 19−20 Oct. 2012. (a) and (b) Surface analysis: mean sea level pressure (solid line, 5 hPa interval) and fronts (warm fronts in red, cold fronts in blue, and occluded fronts in purple) and surface observations and (c) and (d) 500 hPa analysis: geopotential (solid line, 40 gpm interval) and temperature (dashed line, 4°C interval). In (a) and (b), letter **D** (**A**) indicates the centre of low (high) pressure; in (c) and (d), letter **B** (**H**) indicates the centre of low (high) geopotential. Source: Météo-France.

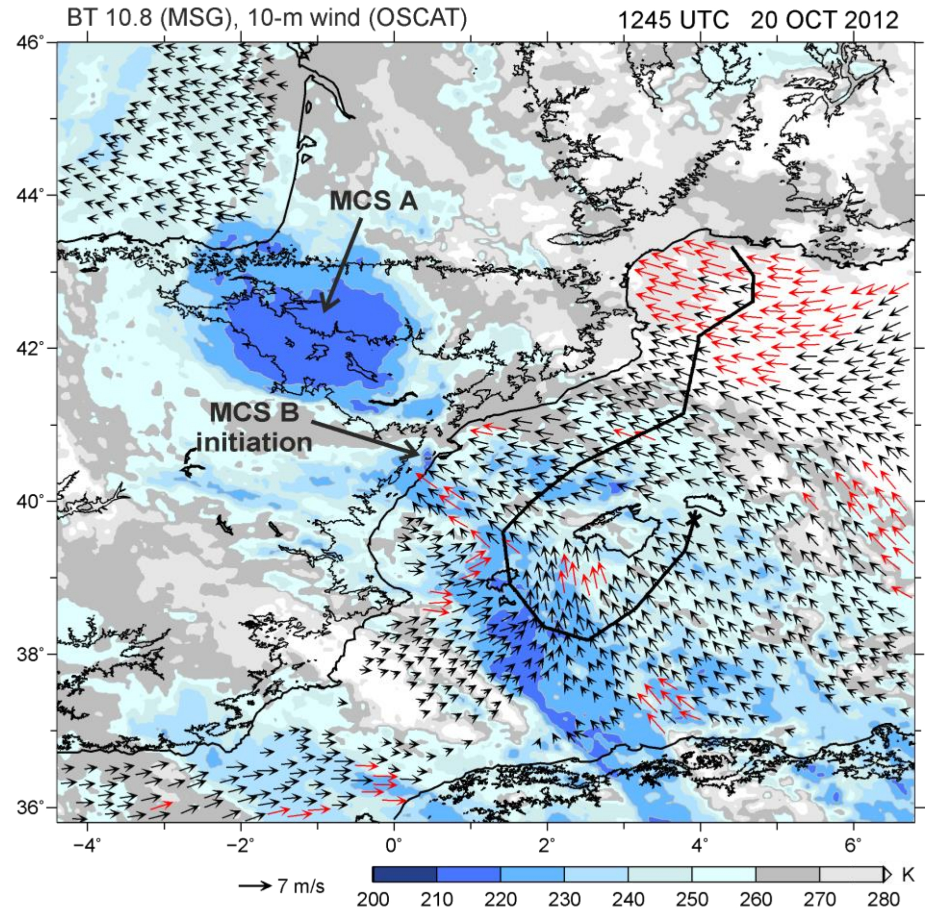

Figure 4. Brightness temperature at 10.8 µm (K) from SEVIRI MSG at 1245 UTC, 20 Oct. 2012 showing the initiation of MCS B and 10 m wind from OSCAT around 1300 UTC. Red vectors show winds stronger than 7 m s^{-1} and black vectors indicate winds below 7 m s^{-1}. The ATR42 aircraft track is shown as the solid black line, and the location of the aircraft at 1245 UTC (3.9°E, 39.8°N, near Minorca) is marked by a cross on the track.

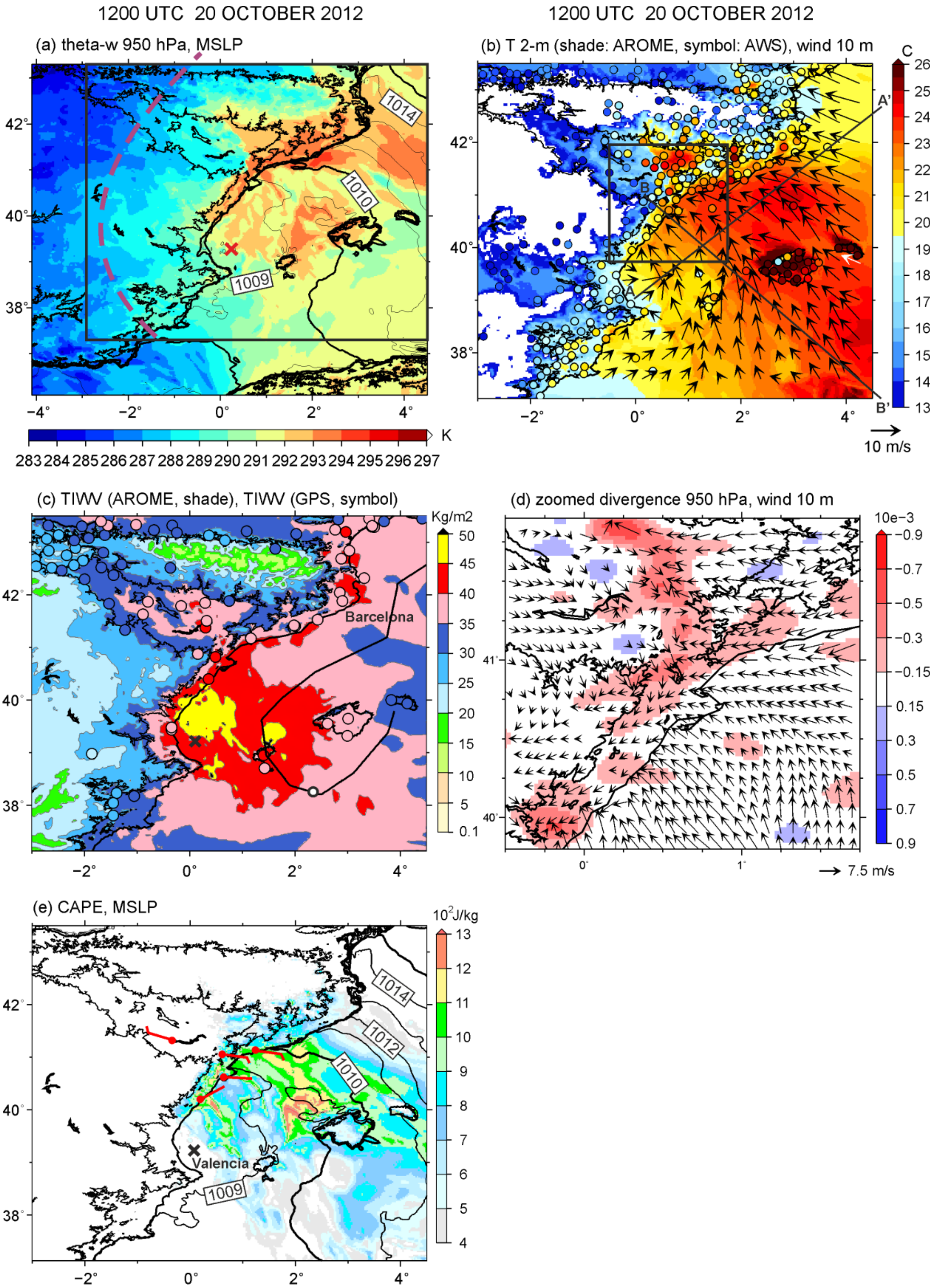

Figure 5. Horizontal distribution at 1200 UTC on 20 October 2012 of (a) AROME-WMED 950 hPa wet-bulb potential temperature (shading) and mean sea level pressure (thin contour every 1 hPa, and thick contour every 5

hPa) (b) AROME-WMED (shading) and AWS observations (coloured dots) of 2 m temperature (shading), and AROME-WMED 10 m winds (vectors, offshore wind only) over the domain shown as a black box in (a). (c) AROME-WMED analysis (shading) and GPS observations (coloured dots) of TIWV. (d) 950 hPa divergence (shading), and 10 m winds (vectors) over the domain shown as a black box in (b). (e) CAPE (shading), MSLP (same contour with (a)), and near surface winds from AWS (red barb, full barb and half barb denote wind speeds of 5 and 2.5 m s^{-1}, respectively). The square in (a) indicates the domain (b), (c), and (e); the square in (b) indicates the domain (d). The cross mark (0.1°E, 37.8°N) in (a), (c) and (e) depicts the location of the minimum of MSLP. In (c), the track of the ATR42 aircraft is shown by the black solid line and the aircraft location at 1200 UTC (2.4°E, 38.3°N) is marked by a white circle.

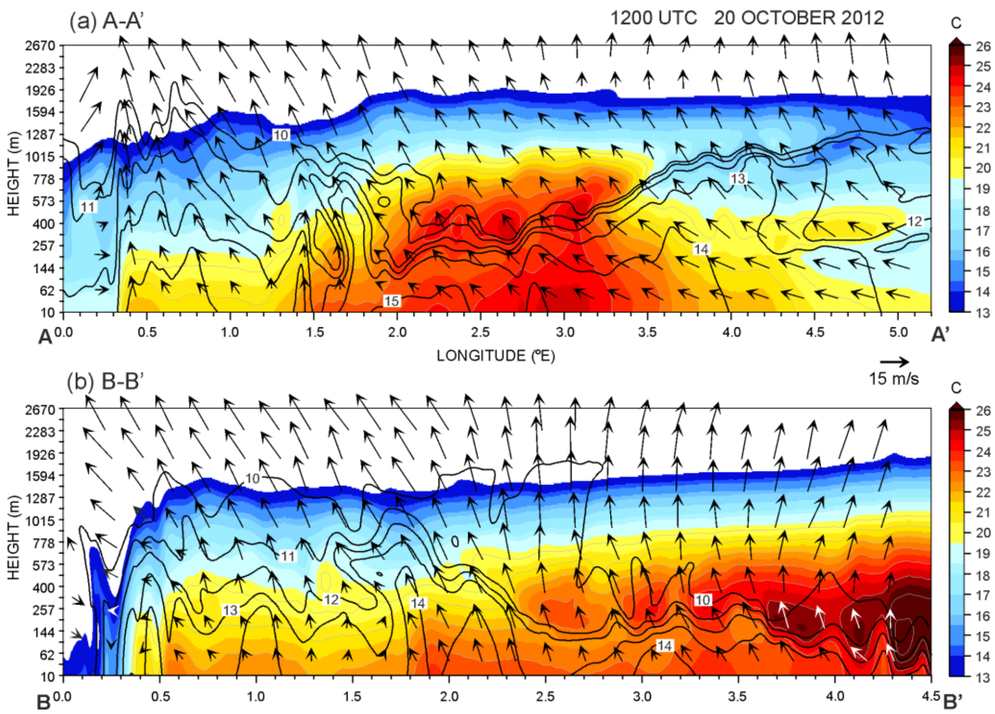

Figure 6. AROME-WMED vertical cross-section of temperature (shading), water vapour mixing ratio (WVMR, contours every 1 g kg^{-1} from 10 g kg^{-1}, and horizontal wind (a) along A-B line from 0°E/39°N (marked as 'A' in Fig. 5b) to 5.2°E/42.3°N (marked as 'A'') and (b) along B-B' from 0°E/41°N (marked as 'B') to 4.5°E/37.1°N (marked as 'B'') at 1200 UTC on 20 Oct. 2012.

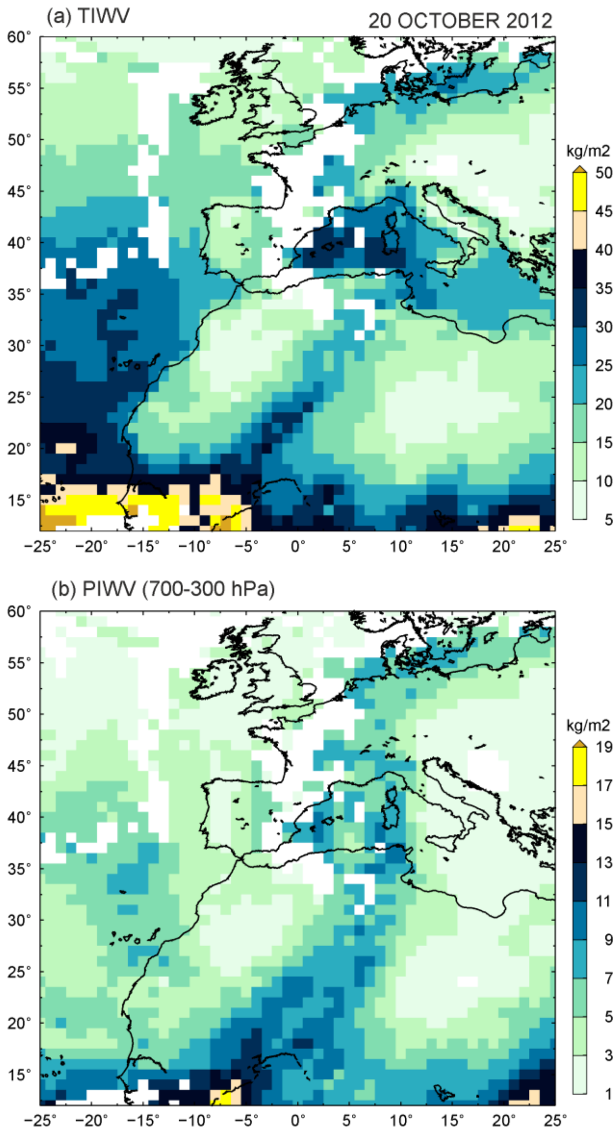

Figure 7. Horizontal distribution of (a) total integrated water vapour content and (b) partial integrated water vapour content between 700 and 300 hPa derived from MODIS/Aqua on 20 Oct. 2012. The MODIS/Aqua Equator-crossing time is 1330 local solar time. The integrated water vapour fields is a composite of MODIS observations acquired between 1153 and 1333 UTC.

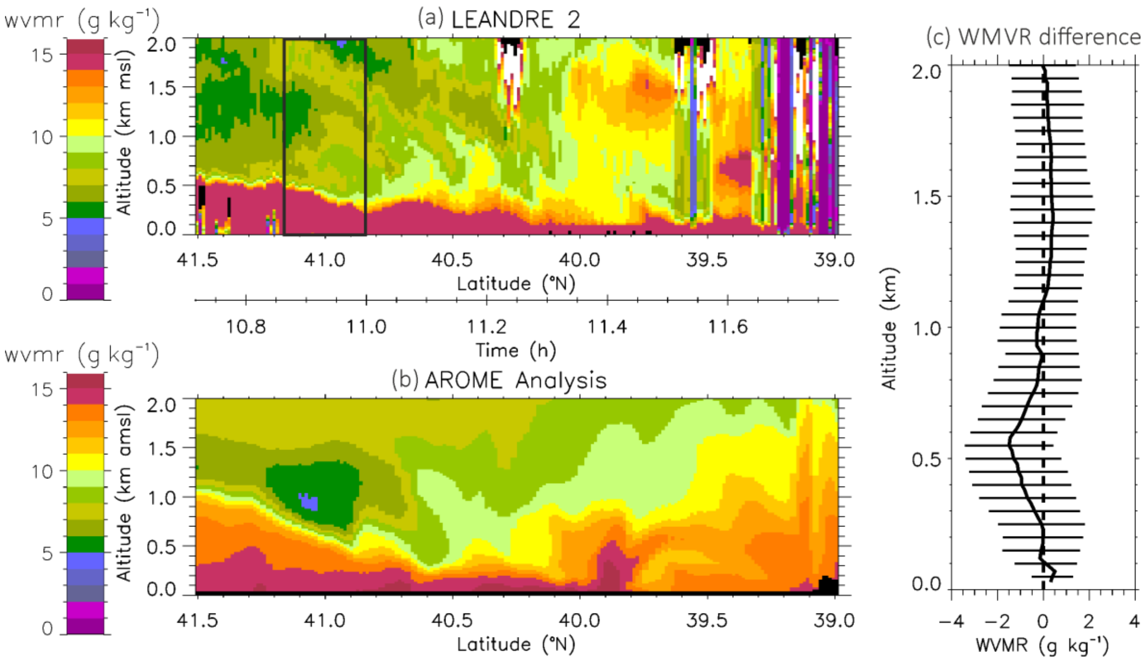

Figure 8. (a) Vertical cross-section of water vapour mixing ratio (WVMR) acquired from LEANDRE 2 along the ATR42 flight track from 41.5°N to 39.0°N (blue line in Fig. 1a). The evolution of WVMR is provided as a function of latitude and decimal time. Lidar data appearing in white are related to the presence of clouds. (b) Same as (a) but for AROME-WMED analysis. WVMR profiles are extracted along the ATR42 flight track at 1200 UTC and location of the LEANDRE 2 WVMR profiles. (c) Comparison between the lidar-derived and AROME-derived WVMR profiles over a box marked in (a) (centered at 3.5°E, 41°N) by a profile of the mean difference (LEANDRE2 minus AROME) for the entire leg 1, together with the standard deviation (horizontal bar).

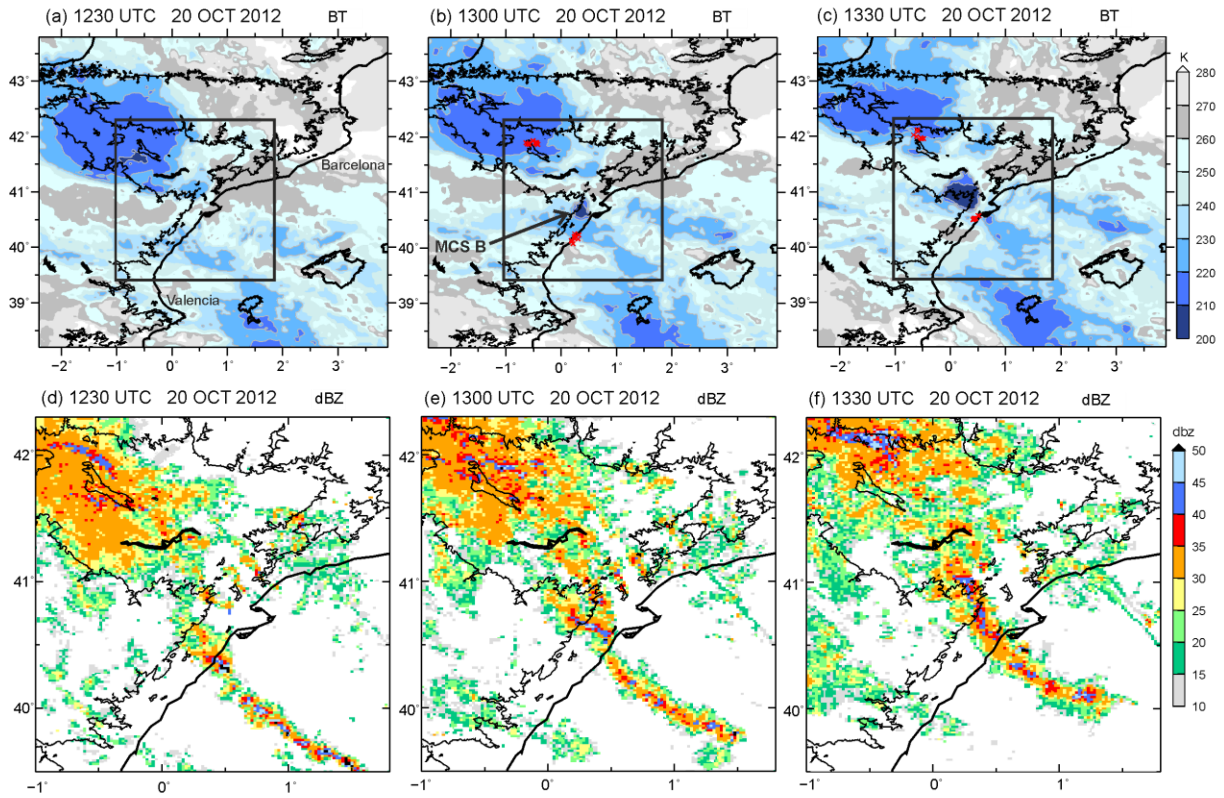

Figure 9. Brightness temperature at 10.8 µm (K) observed with SEVIRI MSG (a)−(c) and surface radar network (d)−(f) from 1230 UTC to 1330 UTC, 20 Oct. 2012. Coastal line and the 500 m terrain height are contoured in each domain. The inner domain in (a)−(c) depicts the domain of (d)−(f). Red crosses in (b)−(c) indicate the location of lightning during the 5 minutes preceding the time of SEVIRI imagery.

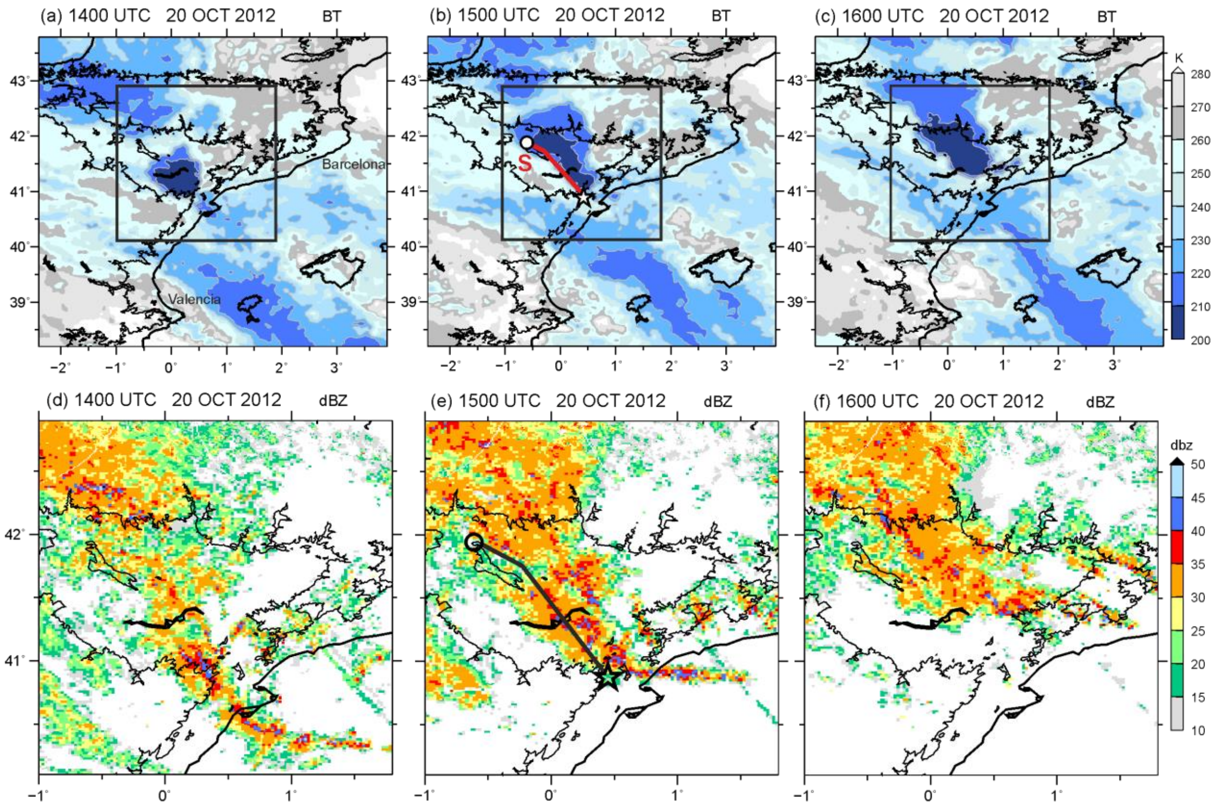

Figure 10. Same as Fig. 9 but for 1400 UTC, 1500 UTC, and 1600 UTC, 20 Oct. 2012. The red line in (b) and the black line in (e) indicate the F20 aircraft flight track from 1435 UTC to 1450 UTC.

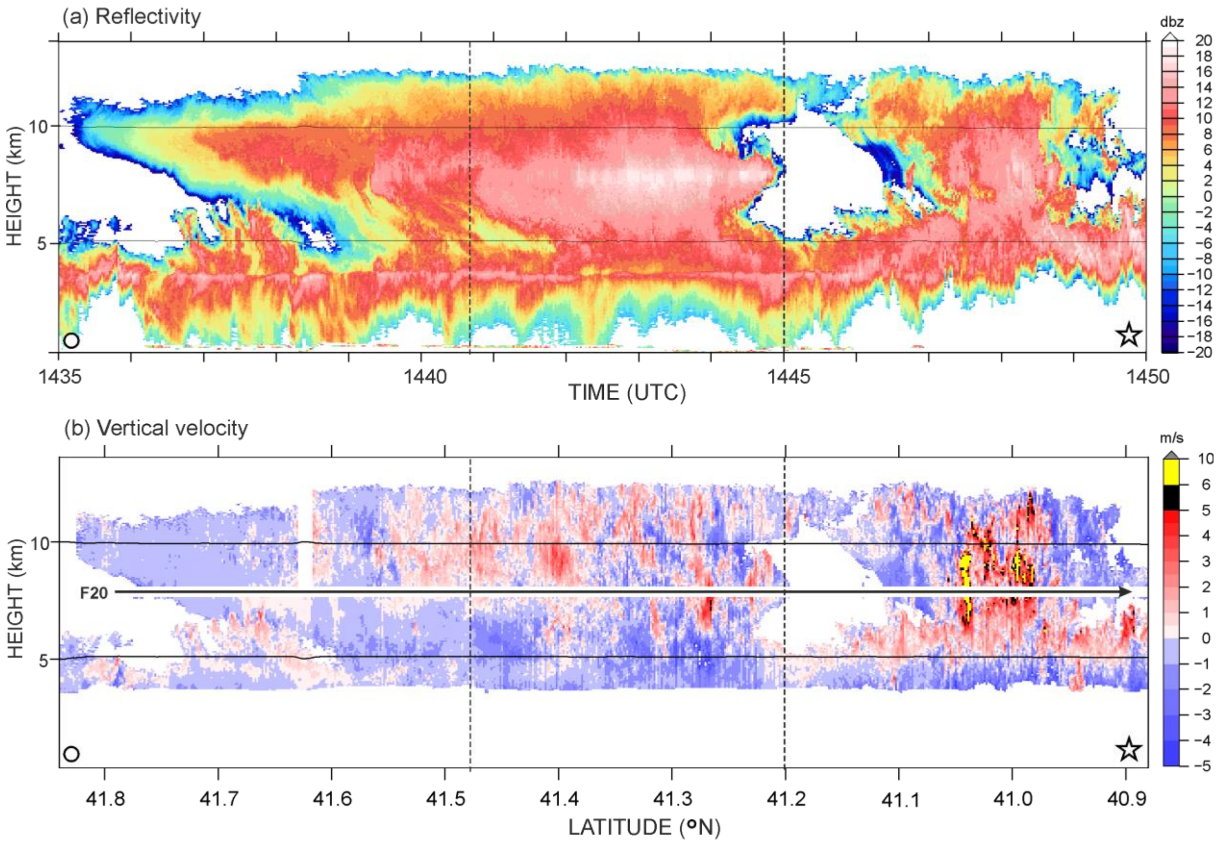

Figure 11. Vertical cross-sections of reflectivity and vertical wind acquired from RASTA radar along the F20 track shown in Fig. 10b and 10e, from 1435 UTC (latitude of 40.9°N; letter **S** with a circle symbol) to 1450 UTC (latitude of 41.82°N; star symbol), 20 Oct. 2012.

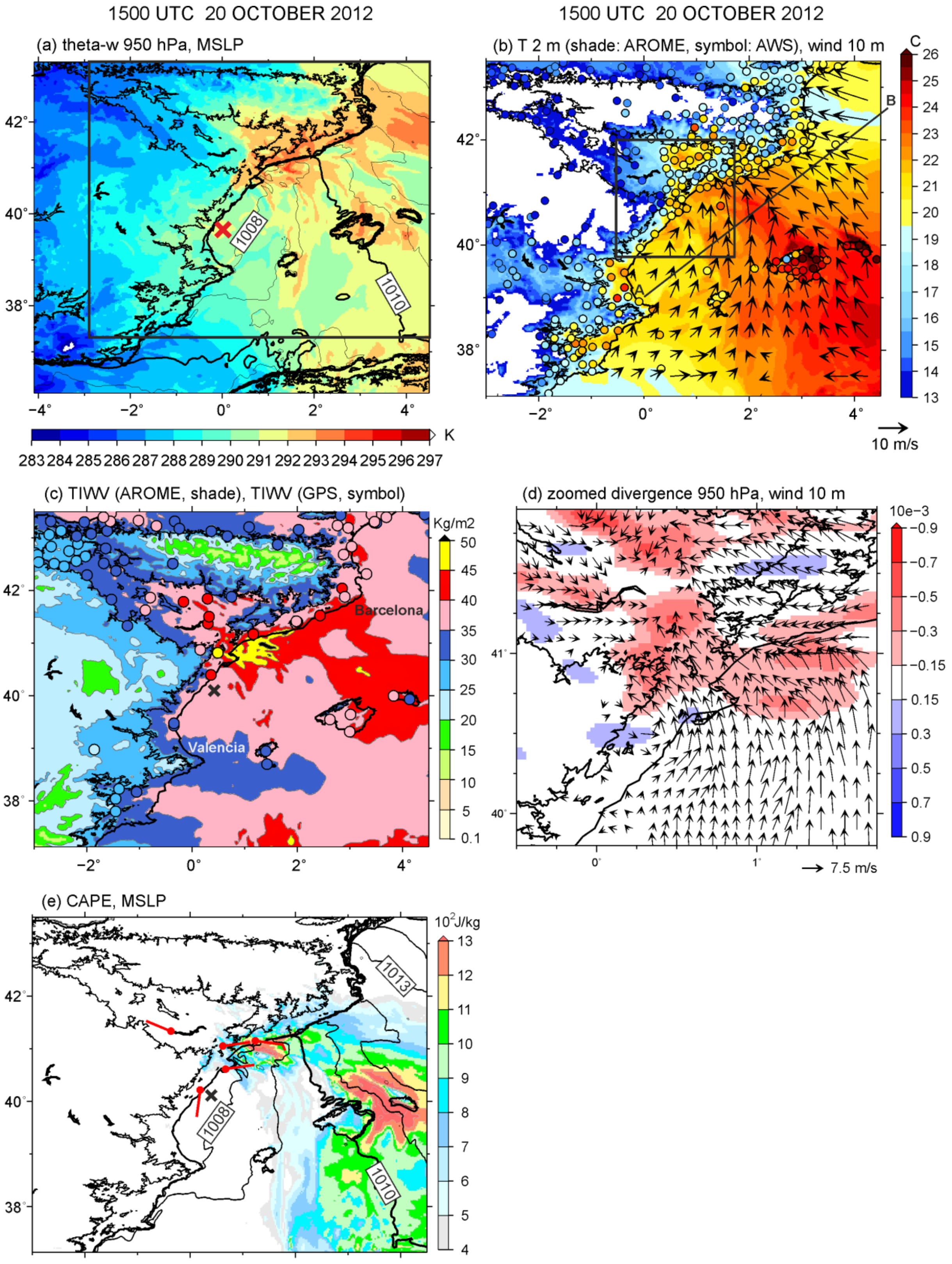

Figure 12. Same as Fig. 5 but for 1500 UTC on 20 October 2012.

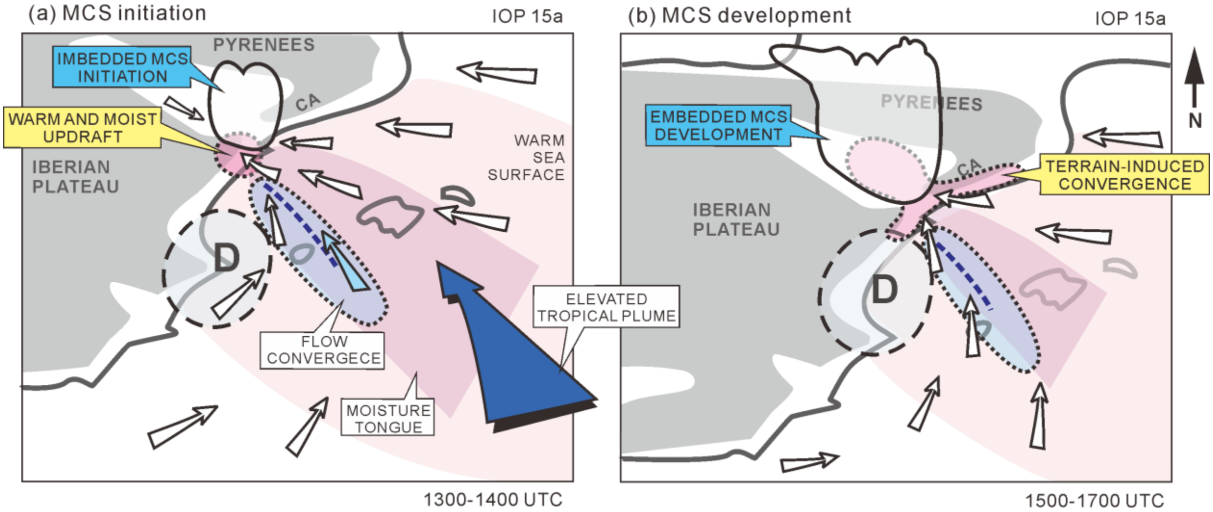

Figure 13. Schematic summarizing the main features and processes responsible for favouring the initiation of MCS B leading to the HPE over north-eastern Spain during IOP 15a. The time at which the frames are valid are also indicated. White arrows indicate the low-level wind (925 hPa). The light blue region (marked **D**) closed by the dashed black line depicts the surface low pressure system. The red region enclosed in the dashed black line shows the warm and moist local convergence. The blue region closed by the dotted black line depicts the cloud cluster including the convergence line (blue dashed line). The blue arrow shows the elevated tropical plume. The grey region indicates the terrain with altitude higher than 500 m. In (a), the blue arrow depicts the accelerated wind between the islands of Ibiza and Majorca (see Fig. 1 for location).